

## HI IMAGING OBSERVATIONS OF SUPERTHIN GALAXIES. I. UGC 7321

JUAN M. USON<sup>1</sup>L. D. MATTHEWS<sup>2</sup>*Submitted to the Astronomical Journal*

## ABSTRACT

We have used the Very Large Array to image the isolated “superthin” galaxy UGC 7321 in the H I line with a spatial resolution of 16'' and a spectral resolution of 24 kHz (5.2 km s<sup>-1</sup>). We have reached a sensitivity of (0.36 – 0.40) mJy/beam per channel, which correspond to a column density of (8 – 9) × 10<sup>18</sup> atoms cm<sup>-2</sup> (1σ). UGC 7321 has a gas-rich disk with  $\mathcal{M}_{HI} = (1.06 \pm 0.01) \times 10^9 d_{10}^2 \mathcal{M}_{\odot}$  and  $\mathcal{M}_{HI}/L_B = 1.0$  ( $d_{10}$  is the distance to UGC 7321 in units of 10 Mpc, the value adopted in this paper), and no detectable radio continuum emission ( $F_{CONT} = 0.41 \pm 0.25$  mJy). The global H I distribution of UGC 7321 is rather symmetric and extends to ~1.5 times the optical radius ( $D_{HI} = 8'.65 \pm 0'.15$  at  $n_{HI} = 3 \times 10^{19}$  atoms cm<sup>-2</sup>). An “integral sign” warp is observed in the H I disk, commencing near the edge of the stellar distribution, and twisting back toward the equatorial plane in the outermost regions. In addition, the position-velocity diagram suggests the presence of a bar or inner arm within ~40'' from the center. The rotation curve of UGC 7321 is slowly rising; it reaches its asymptotic velocity of ~110 km s<sup>-1</sup> at ~2.5' from the center (about 0.9 optical radii) and declines near the edge of the H I disk. The ratio of the inferred dynamical mass to the mass in gas and stars is ~12 d<sub>10</sub><sup>-1</sup>, implying that UGC 7321 is a highly dark-matter dominated galaxy.

*Subject headings:* galaxies: spiral—galaxies: kinematics and dynamics—galaxies: individual (UGC 7321)—galaxies: ISM—ISM: H I

## 1. INTRODUCTION

“Superthin” galaxies appear “needle-like” on the sky because of their edge-on orientation, highly flattened stellar disks ( $a/b \gtrsim 10$ ) and (near) absence of a discernable spheroidal component (Vorontsov-Vel'yaminov 1967). A spectrophotometric study showed them to have gas-rich, optically diffuse disks with little internal absorption, as well as low emission-line intensity ratios and slowly rising rotation curves (Goad & Roberts 1981). Therefore, many of the so-called superthins are late-type, low surface brightness (LSB) disk galaxies seen at high inclination (Matthews, Gallagher, & van Driel 1999; Dalcanton & Bernstein 2000; see also Gerritsen & de Blok 1999). They seem to be among the least evolved disk galaxies in the local universe, having undergone only minimal dynamical heating, star formation, and angular momentum transport (Bergvall & Rönnback 1995; Matthews et al. 1999; Dalcanton & Bernstein 2000). In addition, their orientation and simple structure make superthins ideal laboratories for probing how galaxy disk structure and morphology are influenced by internal and external processes.

Observational and theoretical arguments suggest that

disk structure and thickness are affected by environment (Tóth & Ostriker 1992; Odewahn 1994; Reshetnikov & Combes 1997; Schwarzkopf & Dettmar 2001) and imply that a disk must remain isolated in order to remain “superthin.” This is often observed, as most galaxies with  $a/b \geq 10$  are devoid of close neighbors (Karachentsev 1999; Matthews & van Driel 2000). However, some exceptions do exist (Duc et al. 2000; Hibbard et al. 2001; Matthews & Uson 2002).

Since superthin galaxies are rich in neutral hydrogen (H I) gas (Giovaneli, Avera, & Karachentsev 1997; Matthews & van Driel 2000), imaging observations of the H I (21-cm) line emission can be used to test whether these objects have truly remained isolated throughout their lifetimes. Dynamical timescales of the outer regions of the gaseous disks of galaxies are longer than those of their stellar disks; hence signatures of past perturbations and interactions such as warps and gas asymmetries can be preserved in the H I distribution, even when none are obvious in the stellar disk (Rix & Zaritsky 1995). In addition, high-sensitivity H I observations can uncover the presence of previously unseen gas-rich companions which

<sup>1</sup>National Radio Astronomy Observatory, 520 Edgemont Road, Charlottesville, VA 22903-2475 USA. Electronic mail: juson@nrao.edu

<sup>2</sup>Harvard-Smithsonian Center for Astrophysics, 60 Garden Street, MS-42, Cambridge, MA 02138 USA. Electronic mail: lmatthew@cfa.harvard.edu

(if present) might also play a role in the evolution of these disks.

We can gain further insight into the nature of superthin galaxies by comparing HI images with data obtained at other wavelengths. For example, measurements of the thickness of the stellar and gaseous disks of superthins are of considerable interest in understanding the evolution of these galaxies. While the stellar scale-heights of superthin disks are typically found to be quite small ( $\lesssim 200$  pc, Matthews 2000; but see also van der Kruit et al. 2001), this does not necessarily mean that their gas disks are also unusually thin, since gaseous and stellar disks are affected by different heating processes. Comparison of the structure and scale heights of the gas disks of superthins with those of other types of galaxies should constrain how the dynamically coldest disks are stabilized, and what mechanisms are responsible for heating and supporting their ISM component, especially in the absence of significant energy input from massive star formation (Sellwood & Balbus 1999; Sánchez-Salcedo 2001).

Since the stellar disks of these galaxies remain so thin, internal as well as external heating processes must be suppressed in them, including ‘firehose’ instabilities (Fridman & Polyachenko 1984), bar formation (Mihos et al. 1997), and the development of spiral arms (Noguchi 1987). In addition, their stability requires the presence of a massive dark halo (Efstathiou, Lake and Negroponte 1982). In fact, superthins should be amongst the most dark-matter dominated of disk galaxies (Zasov, Makarov, & Mikhailova 1991; Gerritsen & de Blok 1999). However, constraints on the dark matter content of edge-on superthin disks have been derived for only a few objects such as NGC 4244 (Olling 1996). Existing optical rotation curve studies of superthins typically show a slow rise throughout much of the stellar disk (e.g., Goad & Roberts 1981; Makarov et al. 1997); but only HI observations permit the derivation of the extended outer disk rotation curves which are necessary to constrain the mass models and dark matter halo parameters. For superthins, such analyses are not complicated by the presence of a bulge component, and the mass contributions of stellar disks are expected to be low, making them particularly well-suited for probing the shape of the distribution of dark matter in these galaxies (Olling 1995).

In spite of the unique information that can be gleaned from detailed studies of edge-on spiral galaxies, only a small number of these have been imaged in the HI line with high sensitivity and high spatial and spectral resolution (e.g., Rupen 1991; Olling 1996; Swaters, Sancisi, & van der Hulst 1997; García-Ruiz, Sancisi, & Kuijken 2002). Moreover, with the exception of Olling (1996), the most sensitive HI imaging observations of edge-on galaxies to date have concentrated on massive, luminous systems of mid-to-early Hubble type rather than on moderate-to-low mass and/or LSB systems like the superthins.

This paper is the first in a series describing new high-sensitivity HI imaging observations of superthin galaxies with moderate optical luminosities ( $L_B \sim 10^9 L_\odot$ ), mod-

erate masses ( $V_{ROT} \sim 100 \text{ km s}^{-1}$ ), and highly flattened disks ( $a/b \sim 10$ ). The galaxies that we have observed are undergoing differing levels of perturbation from a companion, ranging from being isolated to being strongly perturbed, and show differing levels of current star formation. In this paper, we present our study of UGC 7321, an isolated superthin galaxy which offers a unique perspective on the ISM structure of an LSB disk viewed edge-on. By comparing its HI properties to those of other LSB and edge-on spiral galaxies, and ultimately, to the results to be presented in our following papers, we aim to address many of the questions discussed above—i.e., to gain clues on the formation histories of pure disk galaxies and probe how environmental factors, interactions, and internal processes influence the structure, evolution, and star formation histories of late-type disk galaxies.

## 2. THE TARGET: UGC 7321

UGC 7321 is a highly inclined ( $i = 88 \pm 1^\circ$ ) Sd spiral galaxy. Its distance is somewhat uncertain, with estimates ranging from  $\sim 5$  Mpc from a kinematical model of the Local Supercluster (Tully, Shaya, & Pierce 1992) to 14.9 Mpc using the *B*-band Tully-Fisher relation (García-Ruiz et al. 2002). One of us (LDM) has used the *Hubble Space Telescope* to obtain images of UGC 7321 in collaboration with J. S. Gallagher (Wisconsin) for a different project. They estimate that UGC 7321 is located at a distance in the range of (7 – 13) Mpc based on the brightest resolved stars. In this paper, we adopt a distance of 10 Mpc for the derivation of physical parameters, and indicate the dependence of our results with distance explicitly by using the symbol  $d_{10}$  to denote distance in units of 10 Mpc. We summarize the optical and near-infrared properties of UGC 7321 in Table 1.

The scale height of the disk of UGC 7321 is one of the smallest ever reported for a galaxy disk (Matthews 2000). UGC 7321 is also unique among the well-studied edge-on spirals because it has an extremely diffuse stellar disk with only minimal patchy dust obscuration and very low internal absorption. Correspondingly, UGC 7321 has very low far-infrared and CO luminosities (Matthews & Gao 2001).

UGC 7321 is a very HI-rich galaxy with a high  $\mathcal{M}_{HI}/L_B$  ratio. Indeed, Haynes et al. (1998) obtained a carefully calibrated (5%) HI spectrum of UGC 7321 with the Green Bank 43 m telescope, which yielded an integrated HI line flux density of  $44.51 \text{ Jy km s}^{-1}$ . Matthews et al. (1999) made a 7-pointing map with the Nançay decimetric radio telescope and showed that the HI gas extends beyond 1.2 times the optical radius. We compare these single-dish observations with our new VLA HI measurements in more detail in Section 5.3.1. It has also been included in the recent study of warps in edge-on galaxies of García-Ruiz et al. (2002) who used observations made for the WHISP survey.

### 3. OBSERVATIONS

We observed UGC 7321 with the Very Large Array (VLA)<sup>3</sup> in C configuration during 2000 May 26 (hereafter Day 1) and 2000 May 30 (Day 2). Since early 1998, the C configuration is a modified version of the original C configuration (3 km maximum baseline) in which the fifth antenna of the North arm is placed at the center of the array thus improving its sensitivity to extended emission. Indeed, it allowed us to “recover” (nearly) all of the “single-dish” HI signal from UGC 7321 (see Section 5.3.1). The observations were obtained during two 8-hour (late-afternoon to mostly nighttime) observing sessions.

To obtain the best possible velocity resolution over the frequency range of interest (defined from the single-dish HI observations), we observed the field centered at the optical position of the galaxy with spectral mode ‘4’ using two pairs of 127 channels with on-line Hanning smoothing; this produced two pairs of 63 nearly-independent, contiguous channels of width 24.4 kHz ( $\sim 5.2$  km s<sup>-1</sup>). For both observing sessions, the first “IF pair” (consisting of separate right and left circular polarizations) was tuned to the known heliocentric velocity of UGC 7321 (407 km s<sup>-1</sup>), while the second “IF pair” was tuned to a central velocity of 650 km s<sup>-1</sup> (on Day 1), and 300 km s<sup>-1</sup> (on Day 2) in order to search for possible dwarf companions or high-velocity gas in the neighborhood of UGC 7321 (see Section 7). Observations of the point source 1221+282 (5 minute “scans” each) were interspersed with observations of UGC 7321 (30 minute scans). The strong source 1331+305 (3C286) was observed twice each day (10 minute scans) in order to obtain good flux calibration. Most of the data on UGC 7321 (720 minutes) were obtained at elevations above 40°. Details appear in Table 2.

### 4. DATA REDUCTION

#### 4.1. Calibration

Because our chosen phase-calibrator (1221+282) turned out to be considerably weaker (0.86 Jy) than the value given in the VLA calibrator list (1.8 Jy) we used a non-conventional path for the data reduction. We generated a pseudo-continuum database by vector-averaging the data for channels 4 through 60 at each time stamp, but only used this file to find and edit corrupted data (mostly due to interference and cross-talk at small spacings as well as a few malfunctioning correlators).

We determined the overall shape of the bandpass as well as the zeroth-order amplitude and phase calibration in one operation using the strong primary calibrator 1331+305 (3C286, which was observed at an elevation intermediate to those corresponding to the observations of UGC 7321). We adopted a flux of 14.7363 Jy at a frequency of 1418.36 MHz, appropriately scaled to the other two frequency settings, as indicated in the VLA calibration manual. This bandpass calibration was applied to all data, which provided the amplitude scale of each frequency

channel as well as an initial calibration of the instrumental phases. As is well known, phase errors increase at the band-edges and prevent an accurate calibration of the affected channels. We found that channels 1–3 and 61–63 could not be calibrated to the accuracy of the 57 central channels. Therefore, we have not used those six edge-channels in the analysis that follows.

Next, we made a (deconvolved) continuum image of the phase-calibrator using the spectral data from channels 4 through 60 with each visibility gridded at the correct “uv-cell.” This image was used for a subsequent “global” amplitude and phase (self) calibration (i.e., one amplitude and phase correction per antenna per scan which was applied to all frequency channels) in which we constrained the average of the amplitudes to remain constant (a global re-scaling by the factor 0.996) and where the averaging time was that of a “scan.” These corrections were subsequently applied to the UGC 7321 visibilities after linear 2-point interpolation (in time) of amplitudes and phases.

These steps completed the calibration of the observations of Day 1, as we obtained two sets of spectral images (“image cubes”) that were free of any noticeable artifacts. In addition, the spectrum of the strongest continuum source in the UGC 7321 field (J1217+2239, with an observed flux density of 64.5 mJy), located at an angular distance of 8’6, did not show any systematic effects and was well-fitted with a constant over both frequency settings.

On the second day, the VLA was not quite as stable as on the first day and we found it necessary to improve on the calibration of the instrumental antenna-based passbands. We followed the operations described above with a secondary calibration of the passband determined with the data obtained on J1221+282 (the phase calibrator). Because of the low flux density of this calibrator (0.86 Jy) and the confusion in the surrounding area ( $\sim 0.3$  Jy) we could only afford to determine one (complex) correction per antenna and per channel for the whole observing run, which was obtained by comparing the visibilities channel-by-channel with the theoretical values obtained from the continuum image of J1221+282 obtained as described above. These corrections were subsequently applied to the UGC7321 data and new image cubes were made. This step was sufficient for the second frequency setting used on this day, but not so for the first frequency setting, as the spectrum through the aforementioned continuum source, J1217+2239, showed significant curvature. Therefore, we were forced to evaluate scan-based corrections to the spectral passband for the main frequency-setting on this day using the observations of J1221+282 (the phase calibrator). However, given the low signal-to-noise ratio per channel of these observations, we could only determine (scan based) global corrections to the passband in the form of 5-th order Chebyshev polynomials using channels 4 through 60 by comparing the so-corrected data to the theoretical visibility function derived from the con-

<sup>3</sup>The Very Large Array of the National Radio Astronomy Observatory is a facility of the National Science Foundation, operated under cooperative agreement by Associated Universities, Inc.

tinuum image of the J1221+282 field determined in the previous step. These corrections were once again applied to the UGC7321 data using linear-interpolation between pairs of observations of 1221+282. The image cube determined after this calibration was free of defects, and the source J1217+2239 discussed above was well fit with a constant.

We have performed a number of tests on the continuum images of our amplitude and phase calibrators and estimate that the uncertainty in the amplitude scale of the images that we present in this paper is about 1%.

#### 4.2. *Imaging of the Continuum Emission*

We used the line-free channels in the second frequency setting (hereafter IF2) of each observation to compute an image of the continuum emission in the vicinity of UGC7321. Because there were 47 such channels on Day 1 and only 23 on Day 2, we proceeded in the following manner. We first made a multi-field (20 fields) image with the data from channels 4–50 from Day 1 using channel-based “3-D” gridding and a robustness factor  $r = 0.7$ , which offers an optimal compromise between noise and resolution when imaging VLA observations obtained with full UV-coverage (Briggs 1995). This yielded a continuum image computed over an effective bandwidth of  $\sim 1.15$  MHz. These images were used to generate phase corrections through self-calibration of the data with a 5 minute averaging interval. Next we subtracted the theoretical visibilities derived from the images on a channel-by-channel basis and subsequently determined the frequency-averaged residual visibilities. The increased sensitivity of these pseudo-continuum visibilities allowed us to recognize some residual low-level contamination which was mostly due to solar interference (in the data obtained in the late-afternoon) as well as cross-talk on short spacings. These data were discarded (about 11% of the visibilities) prior to restoring the (theoretical) contribution of the radio sources determined above. The same procedure was applied to the line-free channels (38–60) in IF2 of Day 2, except that here a 10 minute averaging time was used for the phase-only self-calibration because of the reduced effective bandwidth ( $\sim 0.56$  MHz). Again, about 10% of the visibilities were found to show low-level contamination and discarded. The resulting pseudo-continuum visibilities were combined and a new set of final images (20 fields) was made using a  $2''$  cell-size. The images have a nearly circular synthesized-beam with  $FWHM \sim 15''$  and an rms noise level of  $66\mu\text{Jy}/\text{beam}$  (essentially the theoretical noise level), and are devoid of any noticeable artifacts. The total deconvolved flux is 199 mJy.

#### 4.3. *Imaging of the Line Emission*

It is customary to remove the continuum emission from the visibilities prior to imaging the line emission in the individual channels. This is often accomplished with a visibility-based subtraction of the continuum in which a first-order polynomial is fit to the real and imaginary components of each visibility, and the residuals are used

to make the channel images (Cornwell, Uson, & Had-dad 1992). In our case, there are only four line-free channels at each end of IF1 (channels 4–7 and 57–60) and the limited number of degrees of freedom in the visibility-based subtraction of the continuum results in an artificial lowering of the noise in the images corresponding to those channels (to  $\sim 75\%$  of the theoretical level). Therefore, we have followed an alternate path to compute the channel images, whereby we have made images of the total (line plus continuum) emission in each channel and subsequently determined the line emission as discussed below.

We made twelve image cubes using the combined data from both of our observing dates for IF1. Only the first image cube (which is centered on UGC 7321) contained HI emission; the remaining eleven image cubes were centered on neighboring continuum sources in order to image the total continuum flux in the field properly. We used a  $3''$ -cellsize and a robustness factor  $r = 1$  in order to minimize the noise level while still yielding a reasonable synthesized-beam which was nearly circular with  $FWHM = 16.2'' \times 15.8''$  at position angle  $PA = -34^\circ$ . The deconvolution was deep, to  $0.35 \text{ mJy beam}^{-1}$  ( $\sim 1\sigma$ ) and was followed by a restoration of spurious (isolated) components if the absolute value of the flux inside a six-pixel radius was below  $0.7 \text{ mJy beam}^{-1}$ . The peak deconvolved flux (line plus continuum, uncorrected for primary-beam attenuation) was 480 mJy at 1417.922 MHz. The rms noise was  $0.35\text{--}0.40 \text{ mJy beam}^{-1}$ . This procedure resulted in images that were free of artifacts and did not show a negative bowl surrounding the HI emission.

We made the corresponding sets of twelve image cubes with the data from IF2 for each one of the two observing dates. Because the noise level was 40% higher than for the combined data from IF1, we stopped the deconvolution and “filtered” the spurious components at correspondingly scaled levels.

Next we combined the three image cubes corresponding to the central field at the three observed frequency settings into a global cube with 125 channels in the following way: Channels 1 through 47 correspond to channels 4 through 50 of IF2 from Day 1. Because the IF settings used on Day 1 resulted in overlapping channels that were reasonably aligned (a misalignment of only  $\sim 4\%$ ) channels 48 through 57 are a weighted average of the images in channels 51 through 60 of IF2 (Day 1) and channels 4 through 13 of IF1 (both days) respectively. Most of the weight is attached to the second image in each pair (created from the combined data from both days). This might seem unnecessary and even undesirable, as corresponding channels observed through both IFs (on Day 1) view the same sky-photons, but the VLA backend introduces some noise into the observation which can be reduced somewhat through this average. Care was taken that the weights accurately reflected the loss of independence of the images averaged. Channels 58 through 101 of the global cube were channels 14 through 57 of IF1 (obtained from the combined observations of both days); while channels 102 through 104 resulted from the weighted average of chan-

nels 58 through 60 of IF1 and 37 through 39 of IF2, Day 2, respectively, with weights determined as above. Because the frequency alignment of the channels was somewhat poorer on Day 2 (a misalignment of  $\sim 25\%$ ) here we have only combined line-free channels, so that the small blurring (in frequency) is of no consequence. Finally, channels 105 through 125 of the global cube correspond to channels 40 through 60 of IF2 of Day 2.

We have performed a number of tests on this combined image cube. Figure 1 shows the spectrum at the position of the continuum source J1217+2239 in the combined, global 125-channel cube. It is well fit by a constant  $S = 64.48 \pm 0.04$  mJy with a Chi-square of 123.9 with 124 degrees of freedom. This is an indication that the bandpass correction has been successful in flattening the spectrum and that the amplitude and phase calibrations on the four different IF-Day combinations are consistent to within the noise level reached. It also shows that the deconvolution has been successful in eliminating the bowl around the HI emission that is quite apparent in the raw images and that any residual deconvolution bias is fairly consistent from channel to channel.

We have examined the statistics of the image cube to check for artifacts. The cube is remarkably clean. For example, Figure 2 shows a histogram of the values in planes 48–104 which correspond to IF1 but with the region of HI emission from UGC 7321 excluded (the central  $9' \times 3'$  for planes 52–100). The histogram is as expected from a statistical distribution with the corresponding number of degrees of freedom (values are correlated within any synthesized-beam area). Even more remarkable is the comparison with the histogram in Figure 3, which shows the distribution of values in the central  $9' \times 3'$  for planes 52–100 that had been excluded from Figure 2. The signal is clearly noticeable, but it is also clear that the negative values show the distribution that is expected in the absence of any deconvolution artifacts, such as bowls.

We have determined the continuum emission from this cube in the image-plane by linear fitting of a first-order polynomial to each line-of-sight (pixel) in the cube (Cornwell et al. 1992) after blanking the region that contains the HI emission from UGC 7321. Because of the finite spacial distribution of the HI emission, this procedure results in a larger number of “line-free” channels per line-of-sight than if the subtraction is performed in the visibility domain and the procedure does not alter the noise characteristics of the channel images in a detectable way. This continuum-subtracted cube has been used for the analysis of the HI emission reported in this paper.

Finally, we have made a similar 125-channel image cube following the procedure just described but with a robustness parameter  $r = -1$ . This is closer to uniform weighting and results in a somewhat sharper synthesized beam that is again nearly circular ( $\text{FWHM} \sim 12.4'' \times 12.0''$  at  $\text{PA} \sim -48^\circ$ , with a  $3''$  cellsize). The weighting results in noise levels that are about 40% larger than the corresponding ones for the  $r = 1$  cube and the deconvolution limits and filtering levels were correspondingly scaled.

## 5. ANALYSIS

### 5.1. Continuum Emission

The region around UGC 7321 contains only relatively weak radio continuum sources (Figure 4). The brightest source within the primary beam, J1217+2239, is located  $8.6'$  to the NW of UGC 7321 and has an integrated flux of  $81.5 \pm 0.2$  mJy (after correcting for the attenuation due to the primary beam), in good agreement with the value  $83.9 \pm 2.5$  mJy listed in the NRAO VLA Sky Survey (hereafter NVSS; Condon et al. 1998).

It is clear from Figure 4 that we have failed to detect continuum emission from UGC 7321 itself. The peak value within the (optical) disk of the galaxy is only  $S = 0.2 \pm 0.07$  mJy  $\text{beam}^{-1}$  (formal error) at  $12^h 17^m 33.8^s + 22^\circ 32' 29''$  (J2000). However, because of the uncertainty introduced by the deconvolution of the sidelobes from J1217+2239, the actual uncertainty at this position is somewhat larger.

UGC 7321 was only weakly detected in the FIR by *IRAS* in the  $60\mu\text{m}$  and  $100\mu\text{m}$  bands. Upon examining the *IRAS*  $60\mu\text{m}$  and  $100\mu\text{m}$  survey scans from the NASA/IPAC Infrared Science Archive, we found UGC 7321 to be consistent with a point source in the FIR with  $\text{FWHM} \sim 1'$ . The *IRAS* faint-source catalog indicates flux densities of  $0.344$  Jy at  $60\mu\text{m}$  ( $9\sigma$ ) and  $0.964$  Jy at  $100\mu\text{m}$  ( $5\sigma$ ) which yields a FIR flux of  $2.3 \times 10^{-14}$   $\text{W m}^{-2}$  (using eq. 14 in Condon 1992) and a predicted  $1.4$  GHz continuum flux density of  $\sim 3.1$  mJy (eq. 15 in Condon 1992). To place a meaningful limit on the radio continuum emission from UGC 7321, we have summed the flux in our continuum image (Section 4.2) within a  $1' \times 1'$  box centered at the coordinates quoted above, which yields a flux density of  $0.41 \pm 0.25$  mJy. Given the low significance of the *IRAS* detections, it is perhaps not surprising that the galaxy is not detected in the radio continuum. In addition, some of the FIR luminosity could be due to a contribution from cirrus emission as well as from a weak embedded nucleus. Indeed, Matthews et al. (1999) found a rather red ( $B - R \approx 1.5$ ), compact feature inside the *IRAS* box. Moreover, a low-mass galaxy such as UGC 7321 might be unable to confine cosmic rays with sufficient efficiency and would thus fall short of the prediction from the FIR-radio correlation.

Using the relations given by Condon (1992), the low FIR emission from UGC 7321 yields a rather small estimate of its high-mass star formation rate of  $\sim 0.006 M_\odot/\text{year}$  (for  $M_\star > 5 M_\odot$ ). Such a rate is more than one order of magnitude smaller than the mean value estimated for all UGC galaxies of type Scd-Im (see Roberts & Haynes 1994), confirming that UGC 7321 is a bona fide low surface-brightness spiral galaxy.

### 5.2. Channel Images

Figure 5 shows the images corresponding to the channels that contain detectable HI emission, flanked with one extra channel on each side, overlaid on an *R*-band image of UGC 7321. A number of features of the HI disk and velocity field of UGC 7321 can be seen in these channel

images. For example, the channels covering the velocity ranges  $293.4 - 319.2 \text{ km s}^{-1}$  and  $479.4 - 510.4 \text{ km s}^{-1}$ , clearly show warping of the outer gas layers. In addition, in most of the channel images, the spread in  $z$  of the emission increases with distance from the disk center, which indicates flaring of the gas layer. However, the gas in the most extreme velocity channels is confined to a narrower distribution than at small and intermediate velocities, contrary to the expectation for a pure flaring model (see also Swaters et al. 1997).

It is interesting that in the two channels representing the velocity extrema of the observed HI emission (i.e., corresponding to velocities of  $283.0 \text{ km s}^{-1}$  and  $531.1 \text{ km s}^{-1}$ ), we see gas that is not located at the edge of the HI disk, but rather at smaller galactocentric radii, near the edge of the stellar disk. This is indicative of a falling rotation curve in the outskirts of UGC 7321 (see Section 6.3 below).

### 5.3. Global Properties of the Neutral Hydrogen in UGC 7321

#### 5.3.1. Total HI Content

In order to estimate the total HI content of UGC 7321 and derive a global HI rotation profile, we measured the total HI flux in each of the channel images from our global,  $r = 1$ , cube, after discarding low values (those with absolute value  $\leq 0.5\sigma$ ) and restricting the sum to the pixels corresponding to the galaxy. The corresponding pixels were determined from an initial selection consisting of those pixels which were above the  $2\sigma$  level (where the galaxy is quite distinct) and expanding such areas by successive surrounding bands 3-pixels wide ( $9''$ ) until the enclosed flux converged. For each channel, the selected areas were summed after correction for the attenuation of the primary-beam. We estimated the error in the total HI flux in each channel from the rms noise in that channel, taking into account the correlation introduced by the synthesized-beam and the correction due to the attenuation of the primary beam. The resulting errors are quite small ( $\sim 3 \text{ mJy per channel}$ ).

The resulting global HI profile is shown in Figure 6. Also shown are the profiles obtained with the NRAO 43 m telescope (Haynes et al. 1998) and with the Nançay telescope (Matthews et al. 1999). The three HI profiles match extremely well given the 5% calibration uncertainty (and statistical correction for primary beam attenuation) of the Green Bank data, and the estimated calibration uncertainty of the seven-pointing Nançay spectrum. The total HI flux derived from the present data is  $F_{HI} = 45.3 \pm 0.5 \text{ Jy km s}^{-1}$ , where the error comes from a statistical contribution of  $0.11 \text{ Jy km s}^{-1}$ , an estimated systematic contribution of  $0.36 \text{ Jy km s}^{-1}$  and a global calibration uncertainty of  $\leq 1\%$ . Comparison with the values measured with the 43 m ( $44.51 \text{ Jy km s}^{-1}$ ) and the Nançay ( $47.6 \pm 4.0 \text{ Jy km s}^{-1}$  with 15% calibration uncertainty) telescopes indicates that the measurements reported in this paper have likely recovered most of the HI flux.

The measured brightness temperatures peak at a value of  $T_B = 97.8 \text{ K}$  at the center of the galaxy and at the systemic velocity. The somewhat better resolution image made using a robustness factor  $r = -1$  ( $\text{FWHM} \sim 12''$ ) yields a corresponding peak brightness temperature  $T_B = 118.3 \text{ K}$ . This value is interestingly close to those measured in the Milky Way (Burton 1970) suggesting that the HI spectrum of UGC 7321 might be affected by self-absorption. We have examined cuts along the major and minor axes of the emission at the systemic frequency (which contains the peak values). The latter is well fit by a Gaussian of half-width  $\sim 24''$ , with the data falling short of the Gaussian fit at the center position by  $\sim 2\%$ , indicating only mild self-absorption. Neglecting this leads to an estimate of the total HI mass of UGC 7321 of  $\mathcal{M}_{HI} = (1.06 \pm 0.01) \times 10^9 d_{10}^2 \mathcal{M}_{\odot}$ .

From the global HI profile, we measure velocity widths at 20% and 50% of the peak maximum of  $234.3$  and  $219.8 \text{ km s}^{-1}$ , respectively. The heliocentric recessional velocity (optical definition) determined as the average of the 20%-level values of the global HI profile is  $406.8 \text{ km s}^{-1}$  (Table 3). These values are all in agreement with previous single-dish measurements.

#### 5.3.2. The Total HI Intensity Distribution

The sub-images containing HI extracted as discussed in the previous section have been added to obtain the total HI intensity map of UGC 7321 which is shown in Figure 7, overplotted on a continuum-subtracted  $\text{H}\alpha + [\text{N II}]$  image of the galaxy. The overall HI morphology of UGC 7321 is typical of normal, edge-on spirals. It shows a relatively smooth, unperturbed, symmetric distribution, and we see no obvious enhancements in the HI emission corresponding to the locations of the  $\text{H}\alpha + [\text{N II}]$  emission. At a resolution of  $\sim 16''$ , the peak intensity observed within the galaxy corresponds to  $n_{HI} = 7.3 \times 10^{21} \text{ cm}^{-2}$ , while the maximum observed extent of the HI disk along the major axis is  $8'.65 \pm 0'.15$  at  $n_{HI} = 3 \times 10^{19} \text{ cm}^{-2}$ , or roughly 1.5 times the ( $D_{26}$ ) diameter of the stellar disk. At  $n_{HI} = 1.0 \times 10^{20} \text{ cm}^{-2}$ , we measure an HI diameter of  $8'.15 \pm 0'.05$ .

The slight depression in the HI intensity distribution visible near the optical center of UGC 7321 is possibly due to the mild self-absorption discussed above. Such features are frequently seen in HI images of edge-on spirals. In addition, small HI filaments appear to be protruding vertically from the disk to higher latitudes. These features are discussed further in Section 6.2.2.

#### 5.3.3. The HI Warp

One particularly interesting feature of the total HI intensity map of UGC 7321 is the “integral sign” warp visible in the HI disk. The warp commences near the edge of the stellar disk, reaching a peak amplitude of  $\sim 5''$  on the east side of the disk and  $\sim 10''$  on the west (i.e., roughly 4% of the HI disk radius), before the gas twists back toward the midplane in the outermost regions. These features can be seen clearly in the warp curve shown in Figure 8, where

we have plotted the mean deviation of the H I gas from the disk midplane as a function of radius, measured by fitting single Gaussians to intensity profiles perpendicular to the disk.

Warps with features similar to those of UGC 7321 have now been observed in the H I disk of the Milky Way (Burton 1988) and numerous edge-on spiral galaxies (Sancisi 1976; Briggs 1990; García-Ruiz et al. 2002). Gaseous warps usually originate at the edge of the stellar distribution, which is to be expected because it would seem easier to pull material out from the midplane in regions where the self-gravity is lowest, and because once material becomes displaced from the midplane, dissipational and dynamical-friction forces will cause it to settle back into equilibrium more quickly within the stellar disk than outside of it (e.g., Bottema 1996). However, the outer stellar disk of UGC 7321 is extraordinarily diffuse (Matthews et al. 1999), implying that its self-gravity should be far less significant than in the outer regions of a galaxy like the Milky Way. Therefore, the commencement of the H I warp near the edge of the stellar disk (with essentially no hint of warping being visible in the stars) seems somewhat surprising.

A number of researchers have shown that warps are more commonly seen in galaxies that have companions (e.g., Reshetnikov & Combes 1998), implying that interactions play a role in triggering them. However, UGC 7321 appears to be an unusually isolated galaxy, with no close companions detectable in the optical bands, and no gas-rich companions with  $M_{HI} \gtrsim 10^6 M_{\odot}$  (see Section 7). The nearest optically catalogued neighbors to UGC 7321 are UGC 7236 (type Im), at  $V_{HEL}=945 \text{ km s}^{-1}$  and a projected distance of 115'6 (0.34 d<sub>10</sub> Mpc), and NGC 4204 (type SBdm), at  $V_{HEL}=861 \text{ km s}^{-1}$  and a projected distance of 117'5 (again 0.34 d<sub>10</sub> Mpc). Assuming a typical group speed of 200 km s<sup>-1</sup>, the last encounter of UGC 7321 with one of its neighbors would have taken place at least  $\gtrsim 1.6 \times 10^9$  years ago, even if they were separated only by their (minimal) projected distance. Is it plausible that an encounter with one of these systems could have triggered the warp in UGC 7321?

A consequence of tidal interactions will be to cause heating (thickening) of galaxy disks (e.g., Reshetnikov & Combes 1997). Although the stellar disk of UGC 7321 is (dynamically) much colder than those of typical spiral galaxies, Matthews (2000) has shown that UGC 7321 does show distinct vertical color gradients and a multi-component stellar disk structure, consistent with a disk that has been mildly heated.

Using statistical arguments, Reshetnikov & Combes (1997) suggested that the typical “cooling” time for a disk mildly perturbed by an interaction should be  $\sim 10^9$  years. Hofner & Sparke (1994), who treat warps as discrete bending modes in a disk embedded in a dark halo potential, have developed a formalism to estimate the age of a warp. In UGC 7321, the rotation curve flattens at about 120'' from the center (the Hofner-Sparke  $r_0$ ), the warp commences at about  $r = 150''$  from the center of the disk, the

peak rotational velocity ( $V_{MAX}$ ) is about 110 km s<sup>-1</sup>, the disk scale length ( $h_r$ ) is 2.5 kpc and the disk mass (in gas and stars) is  $1.34M_{HI} + \Upsilon_{\star}L_B$ . In this latter relation, the factor of 1.34 corrects the gas mass for the contribution of helium and  $\Upsilon_{\star}$  is the stellar mass-to-light-ratio. We assume that the contributions of molecular and ionized gas are negligible.

Using the models of Bell & de Jong (2001), we adopt a stellar mass-to-light ratio  $\Upsilon_{\star}=1.0$  based on UGC 7321's  $B - R$  color of 0.97. Then, equation 7 of Hofner & Sparke (1994) leads to an estimate of the age of the warp of  $\sim 10^9$  years. Thus, our estimate does not exclude the possibility that a mild encounter between UGC 7321 and one of its nearest catalogued dwarf neighbors could have occurred  $\sim 10^9$  years ago and triggered its warp (as well as some mild dynamical heating of its disk). Assuming that the timescale for the cooling of the disk is  $\sim 10^9$  years as suggested by Reshetnikov & Combes (1997), such a scenario would have allowed sufficient time for subsequent star formation (and possible gas accretion) to re-establish the very thin young stellar disk that is observed in UGC7321.

Ultimately, self-consistent numerical calculations (including the gas and the stars, as well as a “live” dark matter halo) will be needed in order to gauge whether the amplitude and line of nodes of the warp of UGC 7321 are consistent with its triggering by the passage of one of its dwarf neighbors, and whether a thin, moderate-mass disk like UGC 7321 could have survived such an encounter relatively unscathed.

## 6. THE H I KINEMATICS OF UGC 7321

### 6.1. *The Velocity Field*

We have computed a map of the first moment of the H I emission (representing the H I velocity field) of UGC 7321 from our  $r = 1$  spectral image cube using the standard “cutoff” technique (Rots & Shane 1975). A  $2\sigma$  clipping was applied to the absolute values in the image cube after spatially smoothing the data with a Gaussian kernel of  $FWHM = 33''$  and Hanning-smoothing the data in velocity. In order to maintain a uniform cutoff with respect to the noise, these operations were performed on images uncorrected for primary beam attenuation. The spatial and velocity smoothing were used for the purpose of deciding which pixels to discard; the moment map was made with the full resolution of the input cube. Because of the biases that clipping of any sort can introduce (Bosma 1981), we used the moment-1 map (shown in Figure 9) only to obtain a qualitative impression of the global H I velocity field of UGC 7321. Overall, the velocity field of UGC 7321 is fairly smooth and normal, although some minor irregularities are visible. In the innermost regions, the isovelocity contours exhibit the characteristic “V” shape of a differentially rotating disk, with only a slight asymmetry in the shape of these contours near the eastern and western ends of the disk. The symmetry of these contours about the midplane shows that the (kinematic) major axis of UGC 7321 does not appear to undergo any significant twisting or preces-

sion.

Although the velocity field of UGC 7321 is fairly regular, a mild asymmetry between the receding and the approaching sides is noticeable about half-way through the extent of the optical disk. In addition, at galactocentric radii  $r \gtrsim 75''$ , the isovelocity contours begin to exhibit some curvature at the edges that can be attributed to the warping of the disk. Finally, at the far edges of the disk, we see the most pronounced deviations from purely regular rotation. On the approaching side, the isovelocity contours exhibit their greatest distortion as the terminal velocity of the disk is neared, while the receding side of the disk shows three irregular patches of higher velocity material superimposed on the constant-velocity outer disk region.

## 6.2. Position-Velocity Diagrams

### 6.2.1. The Major Axis P-V Diagram

In Figure 10 we show position-velocity (P-V) diagrams for UGC 7321 along the major axis of the disk (center panel), as well as at heights of  $\pm 15''$ , above and below the midplane. These diagrams were made from unsmoothed data with no averaging applied along the vertical direction.

The overall shape of the P-V diagrams of UGC 7321 is that of a “scaled-down” giant spiral (e.g., M31; Brinks & Shane 1984); although it shows a smaller fraction of its emission near the terminal velocity (along the “flat” part of the P-V diagram) than in most giant spirals, and the peak rotational velocity of UGC 7321 is only about half of that of a system like M31. A large range of gas velocities is observed at all positions across the disk, particularly in the central regions. While similar features are commonly seen in the P-V diagrams of more luminous spirals, many low-mass spiral galaxies with luminosities and rotational velocities similar to those of UGC 7321 exhibit slowly rising, solid-body rotation curves with a much narrower spread of velocities at any given radius [e.g., IC 2233 (Matthews & Uson 2002); NGC 55 (Puche, Carignan, & Wainscoat 1991); NGC 4395 (Swaters et al. 1999)].

One interesting feature of the major axis P-V profile of UGC 7321 is its “figure-8” shape, which is clearly visible in Figure 10. M31 exhibits a similar signature in its major axis P-V curve, and Brinks & Shane (1984) demonstrated that this results from the warping and flaring of its H I disk. As discussed above, the H I disk of UGC 7321 is also warped, and the twisting of its gas disk is likely to be the origin of the “figure-8” shape seen in this galaxy. This can be seen in Figure 9, where the isovelocity contours are found to be predominantly V-shaped in the inner disk regions, but at  $r \sim 75''$  they begin to twist near the edges.

It is also interesting to note that the central panel of Figure 10 suggests the presence of a (small) bar or inner arm that extends from about  $+30''$  to  $-40''$  and manifests itself mainly in the decrease of the H I intensity at  $\sim (-25'', +80 \text{ km s}^{-1})$ . Indeed, in a barred galaxy viewed edge-on, the lack of available orbits for gas near the corotation radius manifests itself as a perturbation in the major-axis P-V diagram (Kuijken & Merrifield 1995). In addition,

the optical H-band major-axis profile shows two distinct “shoulders” at  $\sim \pm 25''$  where the light exceeds that of a pure exponential disk (Matthews et al. 1999, their Figure 3). Given its edge-on orientation it might be difficult to distinguish between a small bar and an inner arm or even confirm their reality. However, should further observations confirm that UGC 7321 is in fact barred, they would challenge the conventional view that bar formation is strongly suppressed in galaxies with low surface densities and large dark matter contents (Mihos et al. 1997).

### 6.2.2. The Minor Axis P-V Diagrams

In Figure 11 we display P-V diagrams extracted at five different cuts parallel to the rotational axis of UGC 7321: along the minor axis ( $r = 0$ ), at  $r = \pm 30''$ , and at  $r = \pm 60''$ . In all of these P-V profiles, we identify features at  $\geq 2\sigma$  levels that appear to be filaments extending out of the plane of UGC 7321 to distances up to  $\sim 60''$  ( $\sim 2.9 d_{10} \text{ kpc}$ ). In addition to these features, other apparent asymmetries are visible in the minor axis P-V profiles when the two sides of the disk are compared. These trends are reminiscent of features reported in the giant, edge-on Sbc galaxy NGC 891 by Swaters et al. (1997), which they attributed to the presence of an H I halo produced by a galactic fountain. As discussed by these authors, detailed modelling is required in order to demonstrate conclusively that the apparent high-latitude extensions are not simply manifestations of a warp or of flaring of the gas disk. An analysis of the high-latitude gas will be reported elsewhere (Matthews and Wood 2002).

## 6.3. The Disk Rotation Curve of UGC 7321

### 6.3.1. Derivation of the Rotation Curve

Commonly used methods of converting P-V data into a true disk rotation curve, such as fitting tilted ring models to the velocity field, extracting major axis cuts along the velocity field, or fitting single, intensity-weighted Gaussians to one-dimensional P-V slices, break down for edge-on and nearly edge-on galaxies as a consequence of projection effects. Indeed, if applied to highly inclined galaxies, these methods will result in a rotation curve which is artificially shallow in the inner regions (Sancisi & Allen 1979). Therefore, we have used a technique that was first introduced to Galactic rotation studies by Shane & Bieger-Smith (1966) which involves the determination of the terminal velocity at a given position,  $v_t$ , from one-dimensional P-V cuts at various radii using an “equivalent rectangular measure” based on the location of the extreme velocity features:

$$v_t = v_m + \frac{1}{F_m} \sum_{v_m}^{v_+} F(v) \Delta v - \frac{\Delta v}{2} - \frac{\sqrt{2\pi}}{2} \sigma, \quad (1)$$

where  $F_m$  is the peak flux density in the profile,  $v_m$  is its corresponding velocity,  $\Delta v$  is the channel separation, and  $v_+$  is the velocity at which the wing of the extreme velocity edge of the line profile drops to zero. The last term



in the equation is a correction that accounts for gas turbulence and was introduced by Burton & Gordon (1978) who also noted that this method is rather insensitive to noise. We make the further approximation that  $\sigma$  is everywhere equal to  $7 \text{ km s}^{-1}$ —the average of the range of  $\sigma \sim (5 - 9) \text{ km s}^{-1}$  observed in normal spiral and quiescent dwarf galaxies (van der Kruit & Shostak 1984; Lo et al. 1993; Olling 1996) and which we also find to be consistent with our data based on Gaussian fits to the extreme velocity envelopes of our one-dimensional P-V cuts. We have ignored any additional corrections for asymmetric drift in UGC 7321, as such corrections for the gaseous components of disks are typically on the order of only a few  $\text{km s}^{-1}$ —i.e. small compared with the uncertainties of applying such corrections (de Blok & Bosma 2002).

The resulting rotation curve is shown in Figure 12. We have indicated on this figure the location of the edges of the stellar disk. The statistical errors of these measurements have a median value of  $0.7 \text{ km s}^{-1}$ , with only two points at the end of the receding side and three points at the end of the approaching side having significantly larger statistical errors of up to  $6 \text{ km s}^{-1}$ . However, the uncertainties are likely to be dominated by systematic errors. We have compared the values that we derived using the “equivalent rectangular measure” to those obtained from fitting “half-Gaussian” functions to the outer part of the profiles in the flat region of the rotation curve and estimate systematic errors of order  $\sim 3 \text{ km s}^{-1}$ .

We see that the rotation curve of UGC 7321 flattens on both sides of the disk, reaching a peak rotational velocity of  $\sim 110 \text{ km s}^{-1}$ , but that it rises rather slowly, not reaching  $V_{max}$  until about half-way through the disk. This is in contrast to high surface brightness spirals, whose rotation curves tend to rise rapidly to their asymptotic value, (e.g., Casertano & van Gorkom 1991).

It is clear from Figure 12 that the rotation curve of UGC 7321 does not exhibit any strong asymmetries or lopsidedness, particularly in the inner regions. It does however show a slight ( $\sim 10\%$ ) difference between the peak amplitudes of the approaching and receding sides of the disk, and the rotation curve is observed to extend about 1 kpc further on the approaching side (see also Figure 10).

Figure 12 shows that near the edge of its HI disk, the rotation of UGC 7321 appears to decline, decreasing by  $\sim 9\%$  from its peak value. Evidence for this decline can also be seen in the major axis P-V plot in Figure 10 and the channel maps in Figure 5. A declining rotation curve was also reported for the thin, edge-on spiral NGC 4244 by Olling (1996). Two possible interpretations of this falling rotation curve in UGC 7321 are that either the dark matter halo of UGC 7321 is truncated near the edge of the HI disk, or that we are seeing a projection effect caused by the warping of UGC 7321. Both interpretations are consistent with the data.

Whenever a slowly rising rotation curve is inferred from HI aperture synthesis measurements, it is of some concern whether the apparent slow rise could be an artifact of beam smearing (Begeman 1989). Indeed, some of the slowly ris-

ing rotation curves reported for LSB galaxies in the literature have been attributed to this effect (Swaters, Madore, & Trewheella 2000; van den Bosch et al. 2000). These rotation curves cannot be used to constrain the shape of dark matter halos, since the inner region is the most critical for distinguishing between the cuspy halos predicted by cold dark matter (CDM) models and dark matter halo models with lower density cores.

In order to gauge the possible effects of beam smearing in the rotation curve of UGC 7321, we have performed two tests. Firstly, we produced a new deconvolved image cube of UGC 7321 using a robustness value of  $-1$  as described in Section 4.3, which yielded a spatial resolution of  $\sim 12''$ , 25% narrower than that of our initial ( $r = 1$ ) derivation. The rotation curve obtained following the steps described above is shown as a dotted line on Figure 12. Aside from the uncertainties caused by the  $\sim 40\%$  higher noise level in the higher resolution data, the agreement between the two rotation curves is excellent. A second check is provided by the comparison of the HI rotation curve of UGC 7321 with the rotation curve derived by Goad & Roberts (1981) from optical ( $H\alpha$ ) emission line spectroscopy (shown with ‘+’ signs on Figure 12). The optical data have much higher spatial resolution than the HI data and hence do not suffer from beam smearing. Given the uncertainties introduced by the more irregular distribution of the HII regions compared with that of the HI gas, the agreement between the HI and  $H\alpha$  rotation curves is quite good, even in the innermost regions. Indeed, maximum deviations are  $\lesssim 5 \text{ km s}^{-1}$  (our spectral resolution). As shown by Matthews & Wood (2001), the effects of internal extinction on the optical rotation curve should be negligible in UGC 7321. We conclude that the effects of beam smearing are insignificant in our derived HI rotation curve of UGC 7321.

### 6.3.2. The Dynamical Mass of UGC 7321

Assuming a spherical mass model for UGC 7321, the dynamical mass of UGC 7321 within radius  $r$  is simply  $M_{DYN}(r) = V^2(r)rG^{-1}$ . Therefore, the mass contained within the radius of the last measured point of the rotation curve (taken to correspond to  $r = 11.5 \text{ d}_{10} \text{ kpc}$ ,  $V = 105 \text{ km s}^{-1}$ ), is  $M_{DYN} \sim 3.2 \times 10^{10} \mathcal{M}_{\odot} \text{ d}_{10}$ . This implies ratios of the total mass to the galaxy’s  $B$ -band luminosity and HI mass, respectively, of  $M_{DYN}/L_B = 29 \text{ d}_{10}^{-1}$  and  $M_{DYN}/M_{HI} = 31 \text{ d}_{10}^{-1}$ . These ratios are 7–8 times larger and 3 times larger, respectively, than the median values found by Roberts & Haynes (1994) for Scd–Sd galaxies, indicating a large dark matter content in UGC 7321. Assuming a stellar mass-to-light ratio in the range  $\Upsilon_{*} = 1.0 - 1.4$ , consistent with the  $B - R$  color of UGC 7321, and a correction to the HI mass of 1.34 for the contribution of helium, the ratio of the dynamical mass to the visible mass in UGC 7321 is in the range  $(11-13) \text{ d}_{10}^{-1}$ , which is again rather large.

We have begun detailed modelling of the underlying distribution of dark matter in UGC 7321. Preliminary results indicate a slight preference for a pseudo-isothermal sphere

over the cuspy distributions suggested by CDM numerical simulations (Navarro, Frenk, & White 1996). In all cases, UGC 7321 is highly dark-matter dominated at all radii beyond  $\sim 1.5$  d<sub>10</sub> kpc.

#### 6.4. The Deprojected Radial HI Distribution of UGC 7321

Because of the high inclination of UGC 7321, the column densities inferred directly from the total-intensity map (Figure 7) represent only projected values rather than the true gas surface densities in the disk. Deprojected gas surface densities are of interest for assessing the star-formation efficiency of UGC 7321 and for comparing its HI distribution to that of other less inclined late-type and LSB spirals.

In order to estimate the deprojected HI surface density in UGC 7321 as a function of radius, we have followed an iterative modelling procedure using the formalism developed by Irwin and her collaborators (the CUBIT software, Irwin & Seaquist 1991; Irwin 1994). This is a non-linear least-squares fitting program that operates on a three-dimensional (HI) spectral-line image cube and is capable of simultaneously determining the underlying density distribution and velocity field. We adopted the observed rotation curve for UGC 7321 (see Section 6.3) and used it to determine the density distribution.

From the fits, we found that we were unable to reproduce the HI density distribution of UGC 7321 with a single-component disk model either Gaussian or exponential in  $r$  and  $z$ . Neglecting the warping and flaring of the gas, we were able to find a reasonable fit to the data using a two-component model: (1) a ring of Gaussian cross-section with a central hole of radius  $30''0$ , a scale-height ( $\sigma$ ) of  $7''7$ , a scale-length of  $93''9$ , and peak density of  $0.19$  atoms  $\text{cm}^{-3}$ ; (2) a Gaussian with scale-height of  $5''4$ , a scale-length of  $123''0$ , and a central density of  $0.06$  atoms  $\text{cm}^{-3}$ . Fixing these parameters, we used CUBIT to compute a face-on rendition of the galaxy and “observed” the intensity distribution along its major axis. Subsequently, we used this model profile in order to scale the observed major axis intensity profile of UGC 7321 to a deprojected (face-on) value which is shown in Figure 13. This profile is in good agreement with the one derived for UGC 7321 by García-Ruiz et al. (2002) from Westerbork data using an Abel inversion technique.

Figure 13 shows that the peak HI surface density in UGC 7321 is only  $\sim 5.8 \mathcal{M}_{\odot} \text{pc}^{-2}$ , somewhat smaller than the mean value of  $10 \mathcal{M}_{\odot} \text{pc}^{-2}$  found in normal surface brightness Sd galaxies by Cayatte et al. (1994) or Broeils & van Woerden (1994). Moreover, it appears that at all radii, the gas surface density in UGC 7321 lies below that required for efficient star formation based on the dynamical criterion of Kennicutt (1989). While this star formation criterion should only be considered an approximation (UGC 7321 is clearly forming some stars), this result is nonetheless consistent with the very low star formation rate implied by its low (optical) surface brightness disk, weak CO emission, and low radio continuum

and far-infrared fluxes. Although the gas surface densities observed in UGC 7321 are very low compared with those of normal spirals, they are however rather similar to the typical (subcritical) HI surface densities seen in other late-type, LSB spiral galaxies (van der Hulst et al. 1993). The deprojected functions indicate a drop in the radial HI surface density distribution of UGC 7321 at  $r \approx 12$  kpc; a step of only one synthesized beam ( $0.8$  kpc) leads to a drop from a deprojected surface density of  $n_{\text{HI}} \sim 2.3 \times 10^{19}$  atoms  $\text{cm}^{-2}$  ( $\sim 0.2 \mathcal{M}_{\odot} \text{pc}^{-2}$ ) to  $\sim 6 \times 10^{18}$  atoms  $\text{cm}^{-2}$  ( $\sim 0.05 \mathcal{M}_{\odot} \text{pc}^{-2}$ ,  $\sim 2\sigma$ ).

#### 7. SEARCH FOR HI COMPANIONS NEAR UGC 7321

We have searched for companions to UGC 7321 within a  $25' \times 25'$  field and over the full velocity range covered by our observations. Visual inspection of the image cube shows no recognizable companions. In addition, we have done a “matched-filter” automated search using a set of Gaussian functions in frequency as our kernel (Uson, Bagri, & Cornwell 1991). For  $\Delta\nu$  in the range (24.4–244) kHz (1–10 channels) we search for an expected signal of the form:

$$\langle \mathcal{A}(\nu_{\circ}) \rangle = \frac{1}{N} \int_{\nu_1}^{\nu_2} S(\nu - \nu_{\circ}) \mathcal{H}_{\Delta}(\nu) d\nu \quad (2)$$

where the kernel has the form

$$\mathcal{H}_{\Delta}(\nu) = \exp[-4 \ln 2 (\nu / \Delta\nu)^2], \quad (3)$$

where  $\nu_1$  and  $\nu_2$  are the edges of the observed band, and the norm  $N$  is

$$N = \int_{\nu_1}^{\nu_2} \mathcal{H}_{\Delta}^2(\nu) d\nu. \quad (4)$$

The noise is weighted by the same kernel and is approximately equal to

$$\langle \sigma_{\nu_{\circ}} \rangle \approx \bar{\sigma}_i N^{-1/2}, \quad (5)$$

which is the value that corresponds to the case in which all image planes have similar noise.

The method is surprisingly efficient at finding signals even if their intrinsic shape is not Gaussian. Indeed, it is a good discriminant of faint extensions to the disk of UGC 7321 as they fade into the noise. When we exclude the galaxy delineated as discussed in Section 5.3.1, a search done with a kernel of width equal to one channel yields a set of amplitudes,  $\mathcal{A}$ , which are nearly Gaussian distributed, with tails extending up to  $\pm 5.5\sigma$ . This is reasonably close to what is expected from statistics only as the image cube has  $1.9 \times 10^6$  degrees of freedom (so that tails up to  $\pm 5.2\sigma$  are expected if the noise is Gaussian distributed). In addition, spurious “absorption” at the  $6.5\sigma$  level is found against the source J1217+2239 discussed in Section 5.1. We have traced this systematic to small positional offsets between the three image cubes (corresponding to the three observational settings) that we have combined to generate the 125 channel image cube. These offsets are a consequence of residual phase noise left behind in the calibration.

Because companions are likely to show H I emission with width of up to  $\sim 40 \text{ km s}^{-1}$ , we have repeated our search with kernels of width 2–10 channels. Even though the smoothing introduced by the kernel decreases the number of degrees of freedom, the algorithm “finds” somewhat more extended distributions with tails that reach  $\pm 6\sigma$ , especially when using kernels with a width of a few (3–7) channels (in addition, the line of sight to J1217+2239 again shows spurious signals due to the image jitter just described). This is likely due to a lack of independence between neighboring channels in excess of the  $\sim 4\%$  expected from Hanning-smoothing, which could be introduced by low-level errors in the VLA backend electronics, as well as by errors in the correction of the spectral bandpass during the data reduction due to insufficient sensitivity (see also Section 4.3). We have verified that these tails have not been introduced because of our decision to image the line emission without prior subtraction of the continuum emission (Section 4.3) by reprocessing the data after performing the customary visibility-based subtraction of the continuum emission (Cornwell et al. 1992). The resulting spectral images agree with the ones described above within the noise; although they have a higher “zero-point” uncertainty due to the small number of line-free channels in IF1. In addition, the rms noise is not uniform, being significantly lower for the four line-free channels at each end that are used to define the continuum.

In addition, the matched filter finds a “signal” at a level of  $\sim 7.4\sigma$  ( $1.23 \pm 0.17 \text{ mJy}$ ); which appears in a single synthesized-beam area with a width of about six channels. We are unable to provide any corroborating evidence that would lead us to believe that this small blip represents real H I emission. Moreover, given that the tail of negative values of  $\mathcal{A}$  reaches down to  $\sim -6\sigma$  for this kernel, we prefer to treat it at this time as spurious excess noise. We have added three standard deviations to its fiducial value and corrected it for the attenuation of the primary beam of the VLA antennas in order to derive a robust upper-limit to the H I mass of the fiducial companions to UGC 7321 located within a radius of 12 minutes of arc ( $36 \text{ d}_{10} \text{ kpc}$ ) of  $\mathcal{M}_{HI} < 2.2 \times 10^6 \text{ d}_{10}^2 \mathcal{M}_{\odot}$ .

Therefore, we find no close H I companion that might be responsible for the warp of UGC 7321 (Section 5.3.3). Even allowing for a significant dark matter component in any such companions to UGC 7321, their total masses would still be below 1% of the inferred total mass of UGC 7321 (Section 6.3.2). Such a mass is likely to be too small to excite a warp via tidal forcing (Hunter & Toomre 1969; Kuijken & García-Ruiz 2001), thus requiring either the warp of UGC 7321 to be quite old (in order to have allowed the perturber sufficient time move outside our search region), or that the warp was excited by some other mechanism.

## 8. SUMMARY

We have presented high-sensitivity H I images of the isolated, edge-on, ‘superthin’ spiral galaxy UGC 7321 with a resolution of 24.4 kHz and a total bandwidth of 3.052 MHz

(125 channels). In the optical, UGC 7321 exhibits a diffuse stellar disk with little dust obscuration, an extremely small global scale height, and no discernible spheroid component. These features indicate that UGC 7321 is a late-type, LSB spiral seen at high inclination. UGC 7321 thus allows us to explore both the radial and vertical structure of the ISM of an ordinary LSB galaxy whose disk has not been recently perturbed.

UGC 7321 shows similar global H I characteristics to other late-type, LSB spirals: It has a gas-rich disk with  $\mathcal{M}_{HI} = (1.06 \pm 0.01) \times 10^9 \text{ d}_{10}^2 \mathcal{M}_{\odot}$ , and an inferred ratio of  $\mathcal{M}_{HI}/L_B = 1.0$  (in solar units), which is at the high end of the observed values for spiral galaxies. Assuming a stellar mass-to-light ratio similar to the sun (based on its global  $B - R$  color) UGC 7321 contains a similar fraction of its visible mass in gas as in stars, suggesting that it has been a relatively inefficient star former. UGC 7321 is undetected in the 21-cm radio continuum ( $F_{CONT} = 0.41 \pm 0.25 \text{ mJy}$ ), which is consistent with its status as a low star formation rate system. Assuming a spherical mass distribution, the ratio of the dynamical mass to the total visible mass (total gas+stars) is  $\sim 12$ , implying that UGC 7321 is a highly dark-matter dominated galaxy.

To first order, the total-H I distribution of UGC 7321 is regular and symmetric with a slight depression near its center, and extends to approximately 1.5 times the stellar radius. The deprojected H I surface density is low (peak value  $\sim 5.8 \text{ M}_{\odot} \text{ pc}^{-2}$ ), which is consistent with other LSB spirals. The outer H I disk of UGC 7321 displays mild flaring in addition to an “integral sign” warp that commences near the edge of the stellar disk. The warped material bends back toward the equatorial plane in the outermost regions. The origin of this warp is still not understood, as UGC 7321 appears to be an isolated galaxy. The nearest known companions to UGC 7321 are two dwarf galaxies, both with projected distances of  $0.34 \text{ d}_{10} \text{ Mpc}$  and  $\Delta V_H > 450 \text{ km s}^{-1}$  which would have had their last encounter with UGC 7321  $\gtrsim 1.6 \times 10^9$  years ago. In addition, the observations described in this paper rule out the presence of any close gas-rich companions with H I masses greater than  $2.2 \times 10^6 \mathcal{M}_{\odot}$  ( $10\sigma$ ) within  $12'$  ( $36 \text{ d}_{10} \text{ kpc}$ ).

The H I disk of UGC 7321 appears thicker and more complex than what a single, cold H I layer confined to the midplane would display. However, the projection effects expected from warping and flaring of the gas layer have to be modelled in order to untangle the three-dimensional structure of the galaxy, which is complicated by its near-edge-on orientation. In addition, we detect filaments of gas extending to distances of up to  $\sim 60''$  ( $2.9 \text{ d}_{10} \text{ kpc}$ ) from the mid-plane in the total intensity H I images and in the position-velocity cuts along the minor axis of the disk, which suggests the presence of high-latitude gas.

The position-velocity plot along the major axis of UGC 7321 displays a “figure-8” pattern that we interpret as a manifestation of the warping of the H I disk. In addition, the diagram reveals the presence of a small bar or inner arm. Overall UGC 7321 has a rather regular H I velocity field with only minor perturbations. Similarly,

the HI rotation curve of UGC 7321 exhibits only a mild asymmetry about the two sides of the disk. The rotation curve rises rather slowly and linearly throughout the stellar disk, indicating a low central matter density; this effect cannot be attributed to the finite spatial resolution of our observations. A peak rotational velocity of  $\sim 110 \text{ km s}^{-1}$  is reached near 0.9 optical radii, and a slight decline in the rotation curve occurs in the last few measured points. Two possible interpretations of this decline are that the dark matter halo of UGC 7321 is truncated near the edge of the HI disk or that we are seeing a projection effect due to the warping of the HI layer.

We are grateful to Eric Greisen for discussions on calibration and imaging issues as well as for updating several of the AIPS tasks needed for this work. We have benefited

from valuable discussions with John Hibbard, Michael Rupen, Mort Roberts, Dave Hogg, Harvey Liszt, Butler Burton, Jacqueline van Gorkom, Michael Pohlen, Jim Condon, Bill Cotton and Dick Thompson. LDM was supported by a Jansky Fellowship at the NRAO and is currently supported by a Clay Fellowship at the Harvard-Smithsonian Center for Astrophysics. This research has made use of: the NRAO-AIPS software package, the NRAO-NVSS survey; the NASA/IPAC Infrared Science Archive and the NASA/IPAC Extragalactic Database (NED) which are operated by the Jet Propulsion Laboratory, California Institute of Technology, under contract with the National Aeronautics and Space Administration; and the Digitized Sky Surveys (DSS), which were produced at the Space Telescope Science Institute under U. S. Government grant NAG W-2166.

## REFERENCES

- Begeman, K. G. 1989, *A&A*, 223, 47  
 Bell, E. F. & de Jong R. S. 2001, *ApJ*, 550, 212  
 Bergvall, N. & Rönnback, J. 1995, *MNRAS*, 273, 603  
 Bosma, A. 1981, *AJ*, 86, 1791  
 Bottema, R. 1996, *A&A*, 306, 345  
 Briggs, D. S. 1995, Ph.D. Dissertation, New Mexico Institute of Mining and Technology, Socorro, NM (<http://www.aoc.nrao.edu/ftp/dissertations/dbriggs/diss.html>), p. 64  
 Briggs, F. H. 1990, *ApJ*, 352, 15  
 Brinks, E. & Shane, W. W. 1984, *A&AS*, 55, 179  
 Broeils, A. H. & van Woerden, H. 1994, *A&AS*, 107, 129  
 Burstein, D. & Heiles, C. 1984, *ApJS*, 54, 33  
 Burton, W. B. 1970, *A&AS*, 2, 261  
 Burton, W. B. 1988 in *Galactic & Extragalactic Radio Astronomy*, ed. G. L. Vershuur and K. I. Kellermann (Springer-Verlag: New York), 295  
 Burton, W. B. & Gordon, M. A. 1978, *A&A*, 63, 7  
 Casertano, S. & van Gorkom, J. H. 1991, *AJ*, 101, 1231  
 Cayatte, V., Kotanyi, C., Balkowski, C., & van Gorkom, J. H. 1994, *AJ*, 107, 1003  
 Condon, J. J. 1992, *ARA&A*, 30, 575  
 Condon, J. J., Cotton, W. D., Greisen, E. W., Yin, Q. F., Perley, R. A., Taylor, G. B., & Broderick, J. J. 1998, *AJ*, 115, 1693  
 Cornwell, T. J., Uson, J. M., & Haddad, N. 1992, *A&A*, 258, 583  
 Dalcanton, J. J. & Bernstein, R. A. 2000, *AJ*, 120, 203  
 de Blok, W. J. G. & Bosma, A. 2002, *A&A*, 385, 816  
 Duc, P.-A., Brinks, E., Springel, V., Pichardo, B., Weilbacher, P., & Mirabel, I. F. 2000, *AJ*, 120, 1238  
 Efstathiou, G., Lake, G., & Negroponte, J. 1982, *MNRAS*, 199, 1069  
 Fridman, A. M. & Polyachenko, V. L. 1984, in *Physics of Gravitating Systems* (New York: Springer)  
 García-Ruiz, I., Sancisi, R., & Kuijken, K. 2002, *A&A*, 394, 769  
 Gerritsen, J. P. E. & de Blok, W. J. G. 1999, *A&A*, 342, 655  
 Giovanelli, R., Avera, E., & Karachentsev, I. D. 1997, *AJ*, 114, 122  
 Goad, J. W. & Roberts, M. S. 1981, *ApJ*, 250, 79  
 Haynes, M. P., Hogg, D. E., Maddalena, R. J., Roberts, M. S., & van Zee, L. 1998, *AJ*, 115, 62  
 Hibbard, J. E., van der Hulst, J. M., Barnes, J. E., & Rich, R. M. 2001, *AJ*, 122, 2969  
 Hofner, P. & Sparke, L. S. 1994, *ApJ*, 428, 466  
 Hunter, C. & Toomre, A. 1969, *ApJ*, 155, 747  
 Irwin, J. A. 1994, *ApJ*, 429, 618  
 Irwin, J. A. & Seaquist, E. R. 1991, *ApJ*, 371, 111  
 Karachentsev, I. D. 1999, *Astron. Lett.*, 25, 376  
 Kennicutt, R. C. 1989, *ApJ*, 344, 685  
 Kuijken, K. & García-Ruiz, I. 2001, in *Galaxy Disks and Disk Galaxies*, ASP Conference Series, Vol. 230, ed. J. G. Funes, S. J. and E. M. Corsini, 401  
 Kuijken, K. & Merrifield, M. R. 1995, *ApJ*, 443, L13  
 Lo, K. Y., Sargent, W. L. W., & Young, K. 1993, *AJ*, 106, 507  
 Makarov, D. I., Karachentsev, I. D., Burenkov, A. N., Tyurina, N. V., & Korotkova, G. G. 1997, *Astron. Lett.*, 23, 638  
 Matthews, L. D. 2000, *AJ*, 120, 1764  
 Matthews, L. D., Gallagher, J. S., & van Driel, W. 1999, *AJ*, 118, 2751  
 Matthews, L. D. & Gao, Y. 2001, *ApJ*, 549, L191  
 Matthews, L. D. & Uson, J. M. 2002, in *ASP Conf. Ser. 276, Seeing Through the Dust*, ed. R. Taylor et al. (San Francisco: ASP), p. 414  
 Matthews, L. D. & van Driel, W. 2000, *A&AS*, 143, 421  
 Matthews, L. D. & Wood, K. 2001, *ApJ*, 548, 150  
 Matthews, L. D. & Wood, K. 2002, *ApJ* (submitted)  
 Mihos, J. C., McGaugh, S. S., & de Blok, W. J. G. 1997, *ApJ*, 477, 79  
 Navarro, J. F., Frenk, C. S., & White, S. D. M. 1996, *ApJ*, 462, 563  
 Noguchi, M. 1987, *MNRAS*, 228, 635  
 Odewahn, S. C. 1994, *AJ*, 107, 132  
 Olling, R. P. 1995, *AJ*, 110, 591  
 Olling, R. P. 1996, *AJ*, 112, 481  
 Puche, D., Carignan, C., & Wainscoat, R. J. 1991, *AJ*, 101, 447  
 Reshetnikov, V. & Combes, F. 1997, *A&A*, 324, 80  
 Reshetnikov, V. & Combes, F. 1998, *A&A*, 337, 9  
 Rix, H.-W. & Zaritsky, D. 1995, *ApJ*, 447, 82  
 Roberts, M. S. & Haynes, M. P. 1994, *ARA&A*, 32, 115  
 Rots, A. H. & Shane, W. W. 1975, *A&A*, 45, 25  
 Rupen, M. P. 1991, *AJ*, 102, 48  
 Sánchez-Salcedo, F. J. 2001, *ApJ*, 563, 867  
 Sancisi, R. 1976, *A&A*, 53, 159  
 Sancisi, R. & Allen, R. J. 1979, *A&A*, 74, 73  
 Schlegel, D. J., Finkbeiner, D. P., & Davis, M. 1998, *ApJ*, 500, 525  
 Schwarzkopf, U. & Dettmar, R.-J. 2001, *A&A*, 373, 402  
 Sellwood, J. A. & Balbus, S. A. 1999, *ApJ*, 511, 660  
 Shane, W. W. & Bieger-Smith, G. P. 1966, *Bull. Astr. Inst. Neth.*, 18, 263  
 Swaters, R. A., Madore, B. F., & Trewhella, M. 2000, *ApJ*, 531, L107  
 Swaters, R. A., Schoenmakers, R. H. M., Sancisi, R., & van Albada, T. S. 1999, *MNRAS*, 304, 330  
 Swaters, R. A., Sancisi, R., & van der Hulst, J. M. 1997, *ApJ*, 491, 140  
 Tóth, G. & Ostriker, J. P. 1992, *ApJ*, 389, 5  
 Tully, R. B., Shaya, E. J., & Pierce, M. J. 1992, *ApJS*, 80, 479  
 Uson, J. M., Bagri, D. S., & Cornwell, T. J. 1991, *ApJ*, 377, L652  
 van den Bosch, F. C., Robertson, B. E., Dalcanton, J. J., & de Blok, W. J. G. 2000, *AJ*, 119, 1579  
 van der Hulst, J. M., Skillman, E. D., Smith, T. R., Bothun, G. D., McGaugh, S. S., & de Blok, W. J. G. 1993, *AJ*, 106, 548  
 van der Kruit, P. C., Jiménez-Vicente, J., Kregel, M. & Freeman, K. C. 2001, *A&A*, 379, 374  
 van der Kruit, P. C. & Shostak, G. S. 1984, *A&A*, 134, 258  
 Vorontsov-Vel'yaminov, B. 1967, in *Modern Astrophysics*, ed. M. Hack (Paris: Gauthier-Villars, Gordon, & Breach), 347  
 Zasov, A. V., Makarov, D. I., & Mikhailova, E. A. 1991, *Sov. Astron. Lett.* 17, 374

TABLE 1  
 VISIBLE AND INFRARED PROPERTIES OF UGC 7321<sup>a</sup>

Parameter	Value
$\alpha$ (J2000.0)	12 17 33.8
$\delta$ (J2000.0)	+22 32 25
Hubble type	Sd IV
Distance (Mpc) <sup>b</sup>	7 – 13
P. A. (deg)	$82 \pm 0.5$
Inclination (deg)	$88 \pm 1$
$a/b$	10.3
$D_{B25.5}$ (arcmin)	5.6
$D_{B25.5}$ (kpc) <sup>b</sup>	$16.3 d_{10}$
$h_{r,R}$ (kpc) <sup>b</sup>	$(2.1 \pm 0.2) d_{10}$
$h_{z,R}(0)$ (pc) <sup>b</sup>	$(150 \pm 20) d_{10}$
$B - R$	0.97
$m_B$	13.8
$M_B$ <sup>c</sup>	-17.1
$L_B(L_{\odot})$ <sup>b</sup>	$1.1 \times 10^9 d_{10}^2$
$\mu_{B,i}(0)$ (mag arcsec <sup>-2</sup> ) <sup>d</sup>	$\sim 23.5$
$S_{FIR}$ (W m <sup>-2</sup> )	$\sim 2 \times 10^{-14}$

<sup>a</sup>Values are from Matthews 2000 (and references therein), with a new correction for foreground extinction where appropriate ( $A_B=0.121$  from Schlegel, Finkbeiner, & Davis 1998; instead of  $A_B=0.040$  from Burstein & Heiles 1984). The errors in the intrinsic physical quantities are formal errors; true uncertainties are dominated by the uncertainty in the adopted distance.

<sup>b</sup>We adopt a distance of 10 Mpc (see text),  $d_{10}$  is the actual distance expressed in units of 10 Mpc.

<sup>c</sup>Corrected for internal and external extinction

<sup>d</sup>Deprojected central surface brightness corrected for internal and external extinction

TABLE 2  
SUMMARY OF UGC 7321 OBSERVATIONS

Parameter	Value
Observing Set-Up	
Array configuration	C
Baseline range (m)	30 – 3385
Observing dates ( $2 \times 8$ hours)	2000 May 26 (Day 1), 30 (Day 2)
Phase center, $\alpha$ (J2000.0)	$12^h 17^m 33.8^s$
Phase center, $\delta$ (J2000.0)	$+22^\circ 32' 25.0''$
Total on-source observing time (min)	740 (720 at elevation $> 40^\circ$ )
Flux calibrator	1331+305 (3C 286)
Phase calibrator	1221+282
Number of IFs	4 [ $2 \times$ (RR, LL)]
Channel width (after Hanning smoothing, kHz)	24.4
Velocity separation of channels ( $\text{km s}^{-1}$ )	$\sim 5.2$
Number of channels per IF	63
Heliocentric center velocity (optical definition, $\text{km s}^{-1}$ )	407.0 (IF pair 1, Days 1 & 2)
...	650.0 (IF pair 2, Day 1)
...	300.0 (IF pair 2, Day 2)
Primary beam <i>FWHM</i> (arcmin)	$\sim 30.6$
Deconvolved Image Characteristics	
Robustness parameter ( $r$ ) <sup>a</sup>	1
Synthesized beam <i>FWHM</i> (arcsec)	$\sim 16.2 \times 15.7$
Synthesized beam position angle (deg)	$\sim -36$
Linear resolution of synthesized beam (kpc) <sup>b</sup>	$\sim 0.8 d_{10}$
RMS noise per channel ( $1\sigma$ , mJy beam <sup>-1</sup> )	0.36 – 0.40
RMS noise in Total-intensity image ( $1\sigma$ , mJy beam <sup>-1</sup> km s <sup>-1</sup> )	$\sim 6$
Limiting column density per channel ( $1\sigma$ , atoms cm <sup>-2</sup> )	$(8 - 9) \times 10^{18}$
RMS noise in HI mass per channel, $M_{\text{HI}}$ ( $1\sigma$ , $M_\odot$ ) <sup>b</sup>	$(4.5 - 4.9) \times 10^4 d_{10}^2$

<sup>a</sup>We also used  $r = -1$  ( $FWHM = 12.4'' \times 12.0''$ ,  $PA = \sim -48^\circ$ ) to make higher-resolution spectral images and  $r = 0.7$  ( $FWHM = 15.3'' \times 15.0''$ ,  $PA = -28.4^\circ$ ) to make the continuum image (see sections 4.3 and 4.2, respectively).

<sup>b</sup> $d_{10}$  is the distance to UGC 7321 expressed in units of 10 Mpc (the distance to UGC 7321, see Table 1).

TABLE 3  
21-CM RADIO PROPERTIES OF UGC 7321

Parameter	Value
Measured Parameters	
Peak HI column density (16'' resolution, atoms cm <sup>-2</sup> )	$7.3 \times 10^{21}$
$D_{HI}$ (arcmin) <sup>a</sup>	$8.15 \pm 0.05$
$\theta_{HI,b}$ (FWHM, arcsec) <sup>b</sup>	$16.7 \pm 0.3$
$(a/b)_{HI}$ <sup>c</sup>	29
$\int F_{HI}d\nu$ (Jy km s <sup>-1</sup> )	$45.3 \pm 0.5$
$W_{20}$ (km s <sup>-1</sup> ) <sup>d</sup>	234.3
$W_{50}$ (km s <sup>-1</sup> ) <sup>d</sup>	219.8
$V_{hel,HI}$ (optical definition, km s <sup>-1</sup> )	406.8
$F_{cont}$ (21 cm) (mJy)	$0.41 \pm 0.25$
Derived Quantities	
$M_{HI}$ ( $M_{\odot}$ ) <sup>e</sup>	$(1.06 \pm 0.01) \times 10^9 d_{10}^2$
$M_{DYN}$ ( $M_{\odot}$ ) <sup>f</sup>	$3.2 \times 10^{10} d_{10}$
$M_{HI}/L_B$ ( $M_{\odot}/L_{\odot}$ )	1.0
$M_{DYN}/M_{HI}$	$31.0 d_{10}^{-1}$
$D_{HI}/D_{B25.5}$	1.5

<sup>a</sup>Measured at a column density of  $10^{20}$  cm<sup>-2</sup>.

<sup>b</sup>Projected thickness of HI layer along minor axis measured at a column density of  $10^{20}$  atoms cm<sup>-2</sup> and corrected for the resolution of the synthesized beam.

<sup>c</sup>Axial ratio of HI disk measured at a column density of  $10^{20}$  atoms cm<sup>-2</sup> and corrected for the resolution of the synthesized beam.

<sup>d</sup> $W_P$  is the HI profile width measured at P% of the peak value

<sup>e</sup>Assuming the HI is optically thin (but see Section 5.3.1),  $d_{10}$  is the distance to UGC 7321 expressed in units of 10 Mpc (the distance to UGC 7321, see Table 1).

<sup>f</sup>From  $M_{DYN} = 2.326 \times 10^5 r V^2(r)$ , where we have taken  $r = 11.5$  kpc and  $V(r) = 105$  km s<sup>-1</sup>.

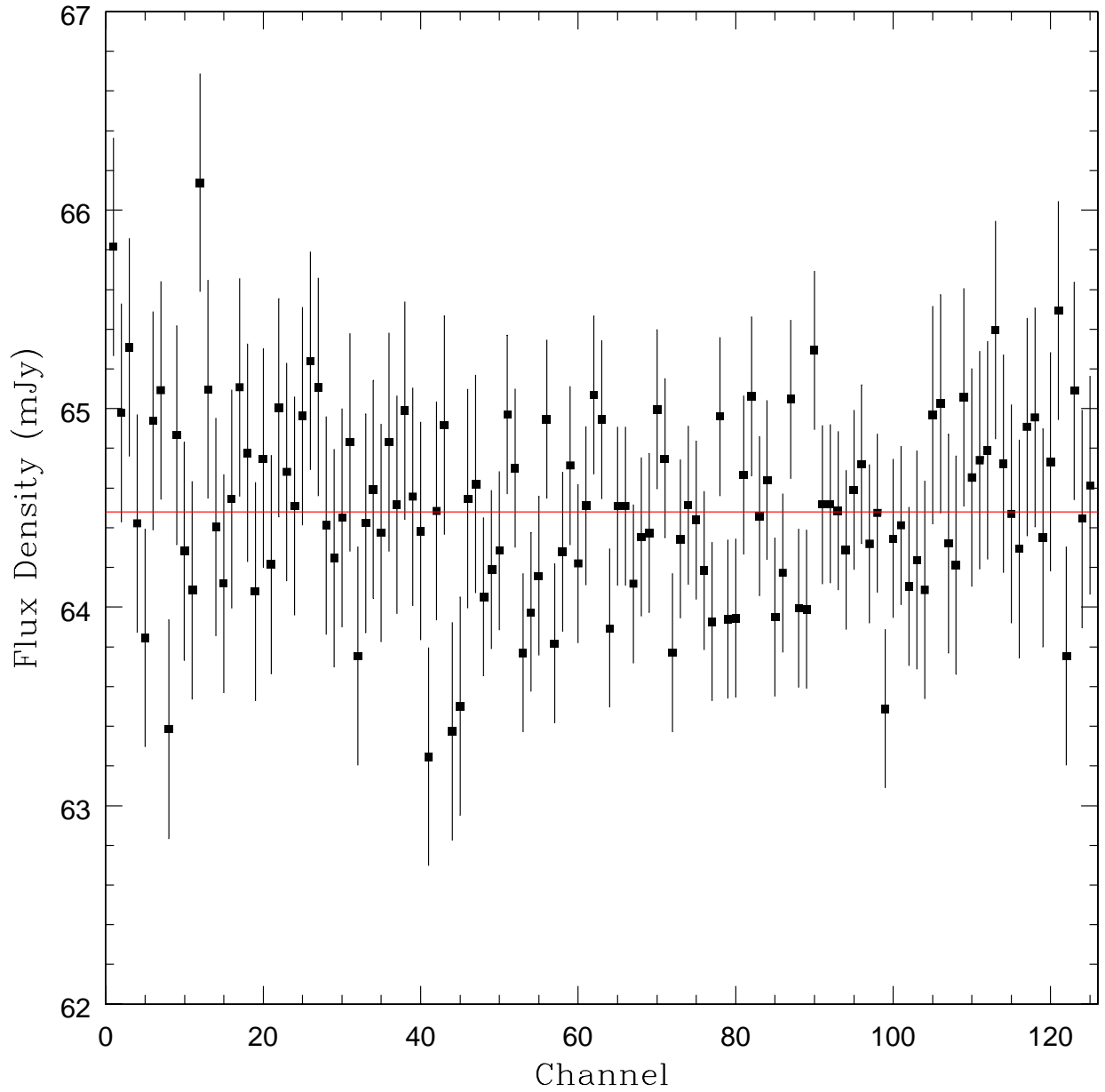


FIG. 1.— Observed spectrum of J1217+2239, the strongest continuum source in the vicinity of UGC 7321. The rms noise is  $\sim 0.54$  mJy for channels 1–47 and 103–125, and  $\sim 0.38$  mJy for channels 48–102. The data are well fit by a constant value of  $S = 64.48 \pm 0.04$  mJy (solid line). No correction for primary-beam attenuation has been applied.



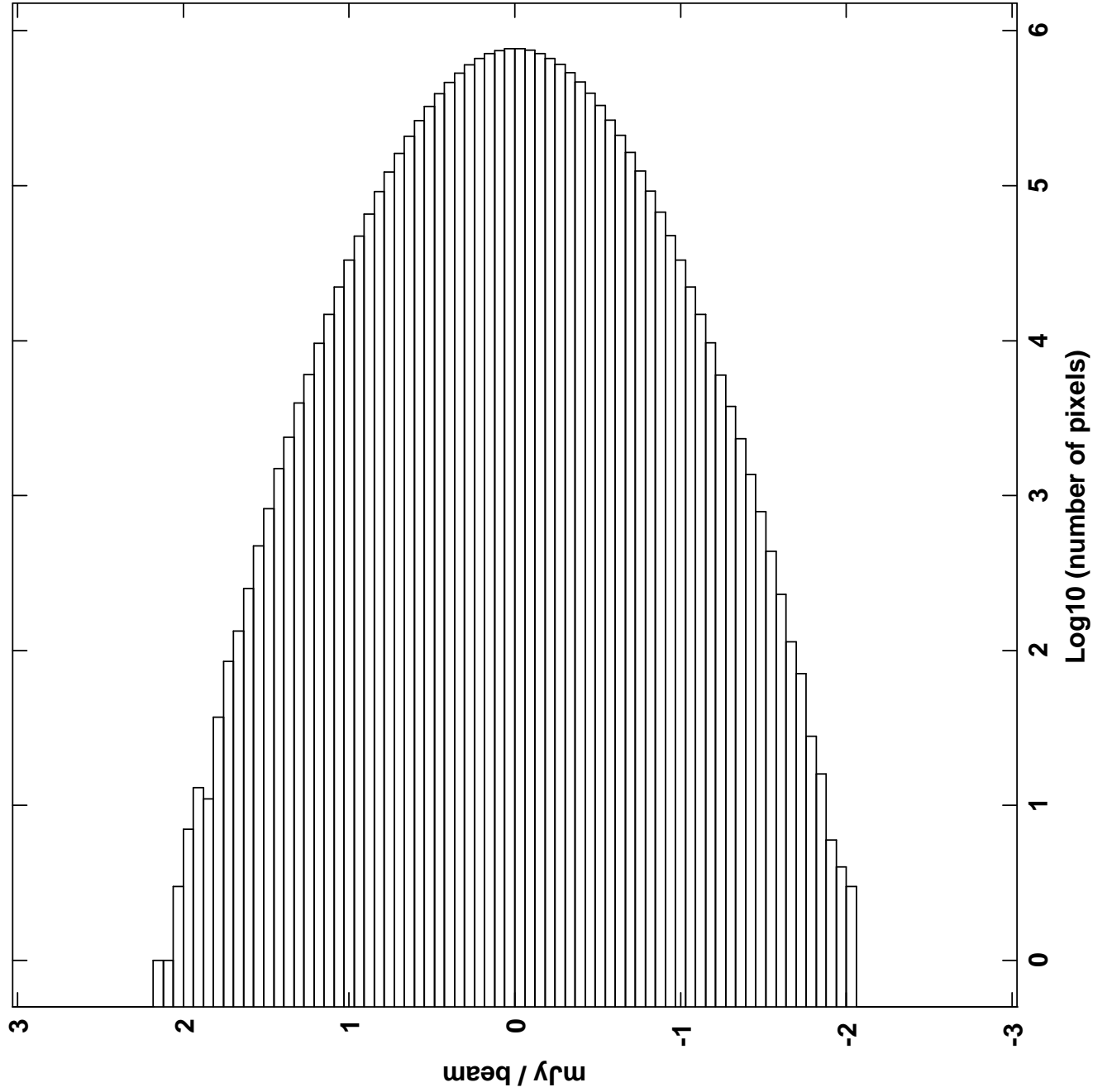


FIG. 2.— Histogram showing the noise distribution in the image-planes of UGC 7321 corresponding to the IF1 setting. These are planes 48–104. The central region ( $9' \times 3'$  for planes 52–100) which contains the H I emission signal has been excluded.

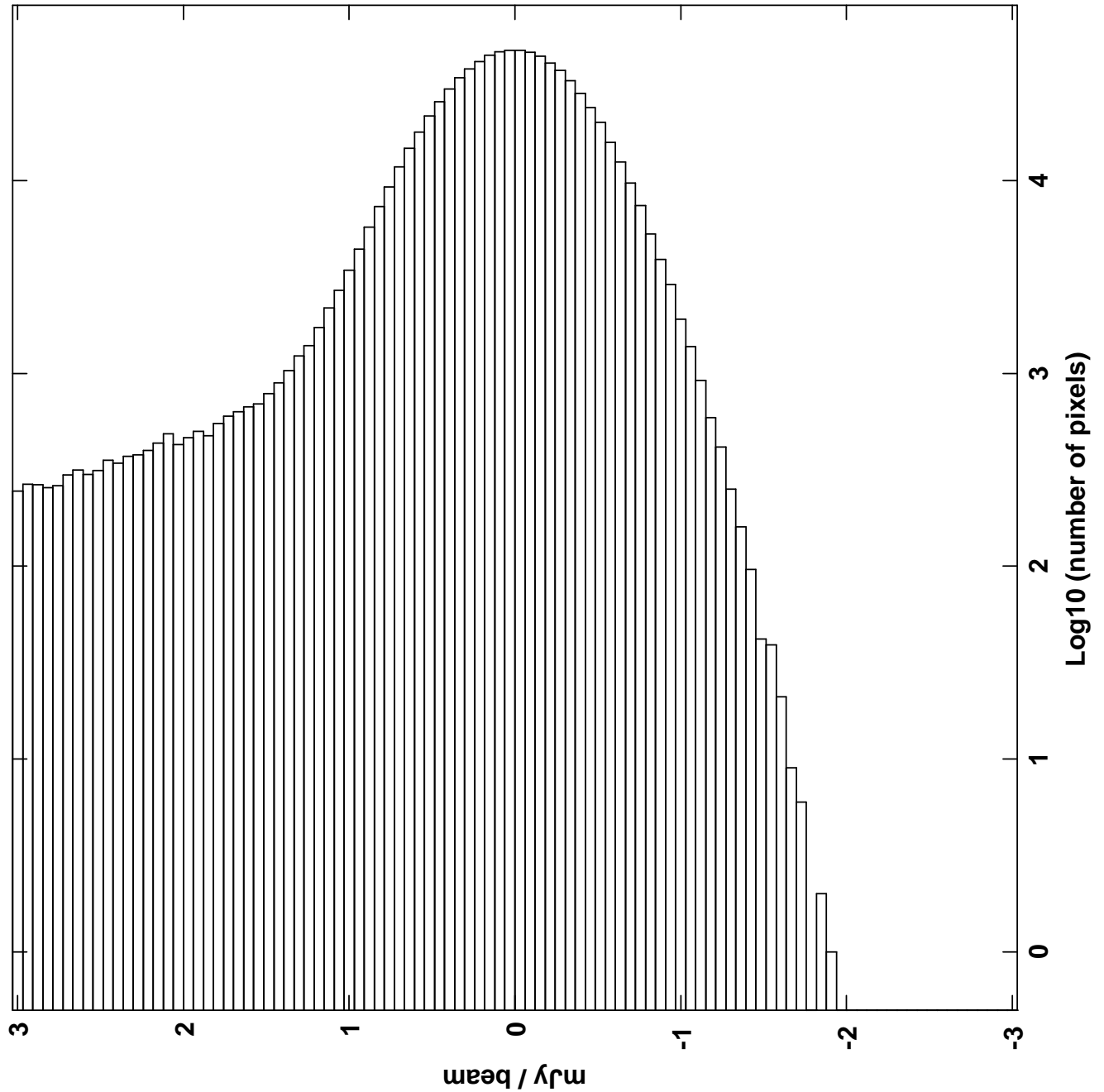


FIG. 3.— Histogram showing the distribution of flux in the central region ( $9' \times 3'$  for planes 52–100) which contains the observed HI emission. Notice the positive tail due to the signal; but also that the negative values show the distribution that is expected in the absence of artifacts.

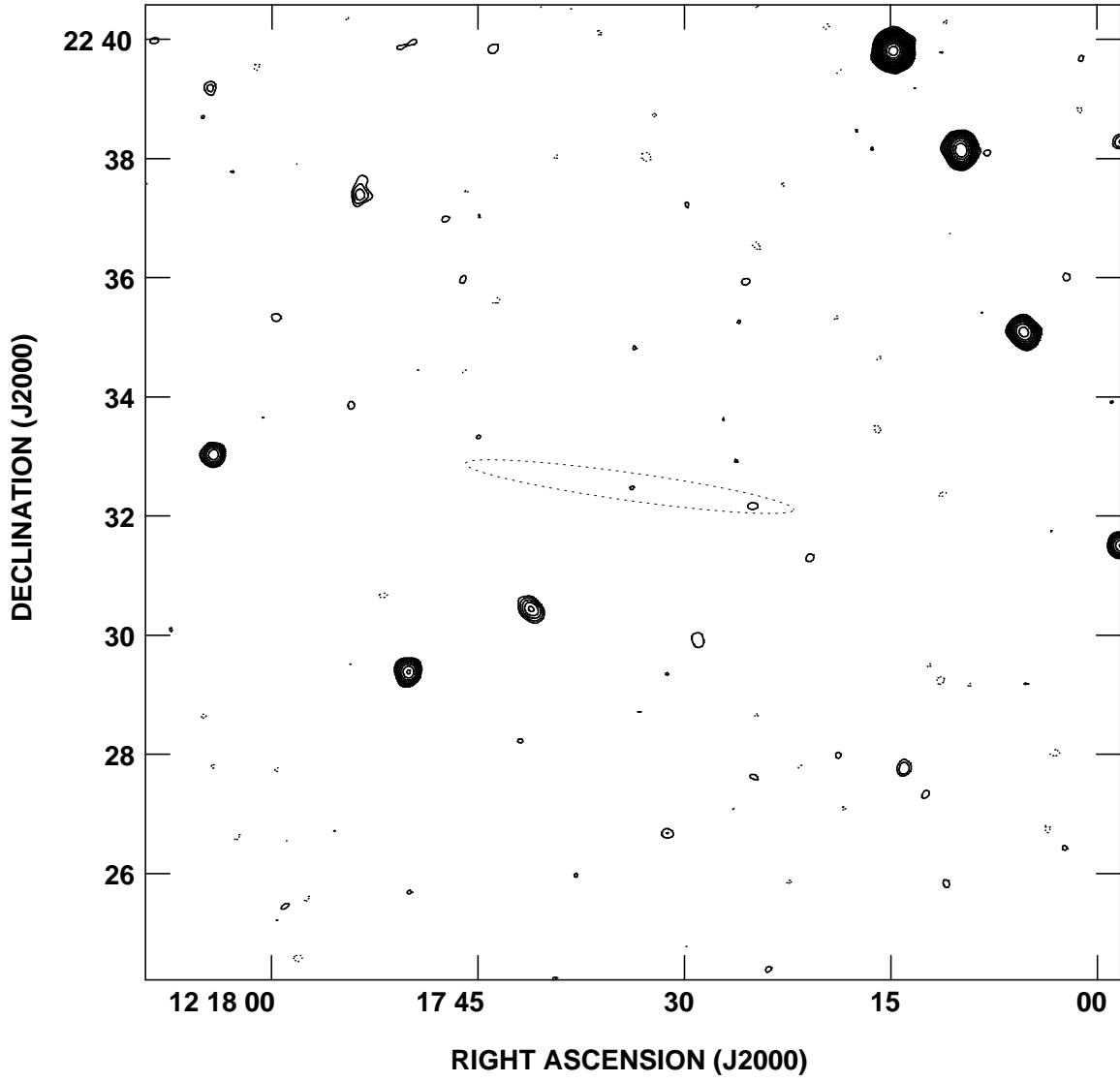


FIG. 4.— Image of the continuum emission in the  $16.4' \times 16.4'$  region centered on the position J1217+2232 at an effective frequency of 1418.0 MHz. The dotted line shows the location of the edge of the optical disk of UGC 7321. Contour levels are [-2 [absent], -1.4, -1, 1, 1.4, 2, 2.8, 4, 5.6, 8, 11, 16, 22, 32, 44, 64, 88, 128, 176, 256, 352] $\times 0.2$  mJy beam $^{-1}$  (the  $3\sigma$  level)].

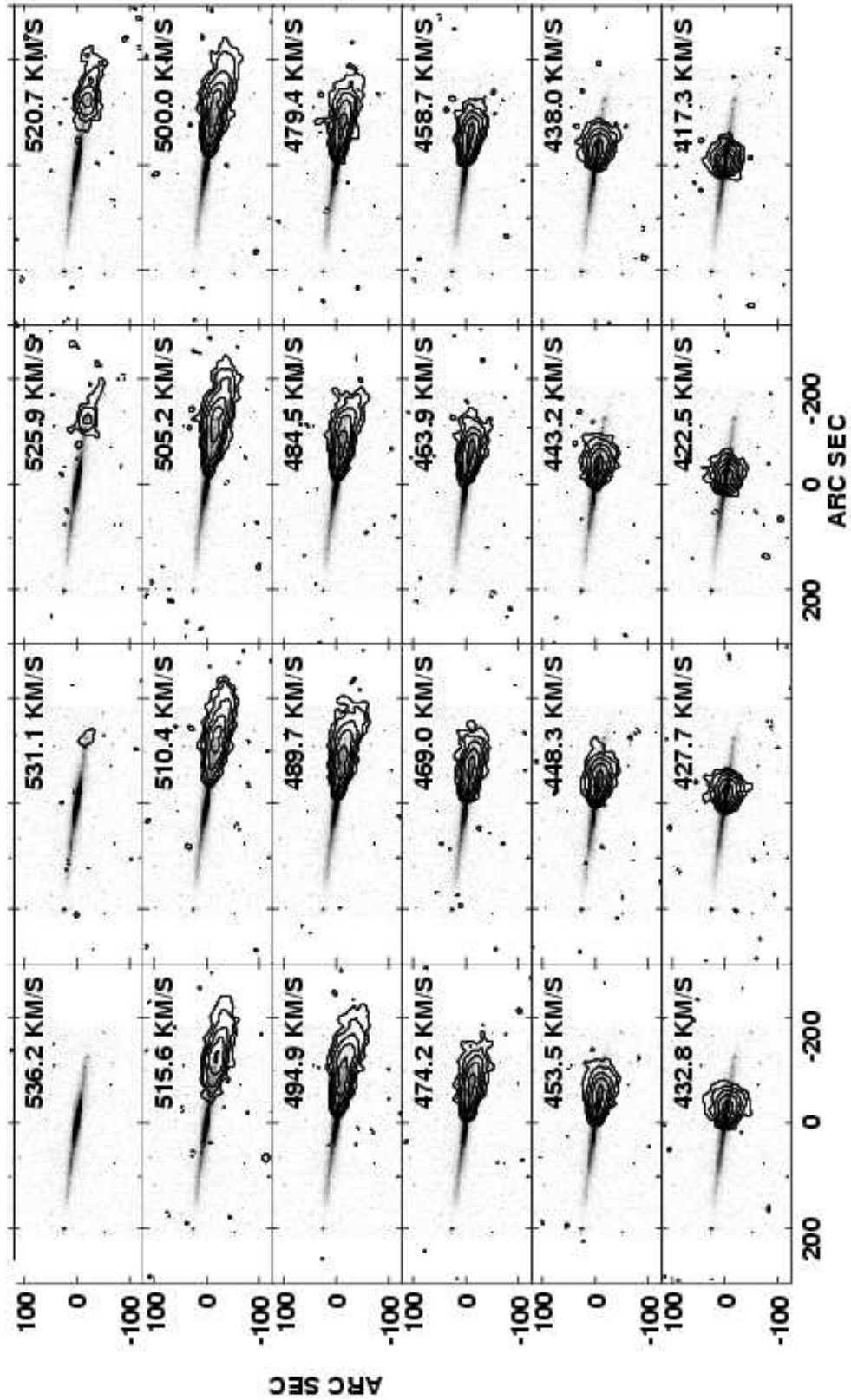


FIG. 5.— HI channel maps of UGC 7321, overlplotted on optical *R*-band images of the galaxy. The maps have a spatial resolution of  $\sim 16''$  and a velocity resolution of  $\sim 5.2 \text{ km s}^{-1}$ . The contours are  $(-2 [\text{absent}], -1, 1, 2, 4, 8, 16, 32) \times 1.2 \text{ mJy beam}^{-1}$ . Only the channels showing line emission (plus one additional channel on either side) are plotted. Each panel is labelled with its corresponding central heliocentric velocity.

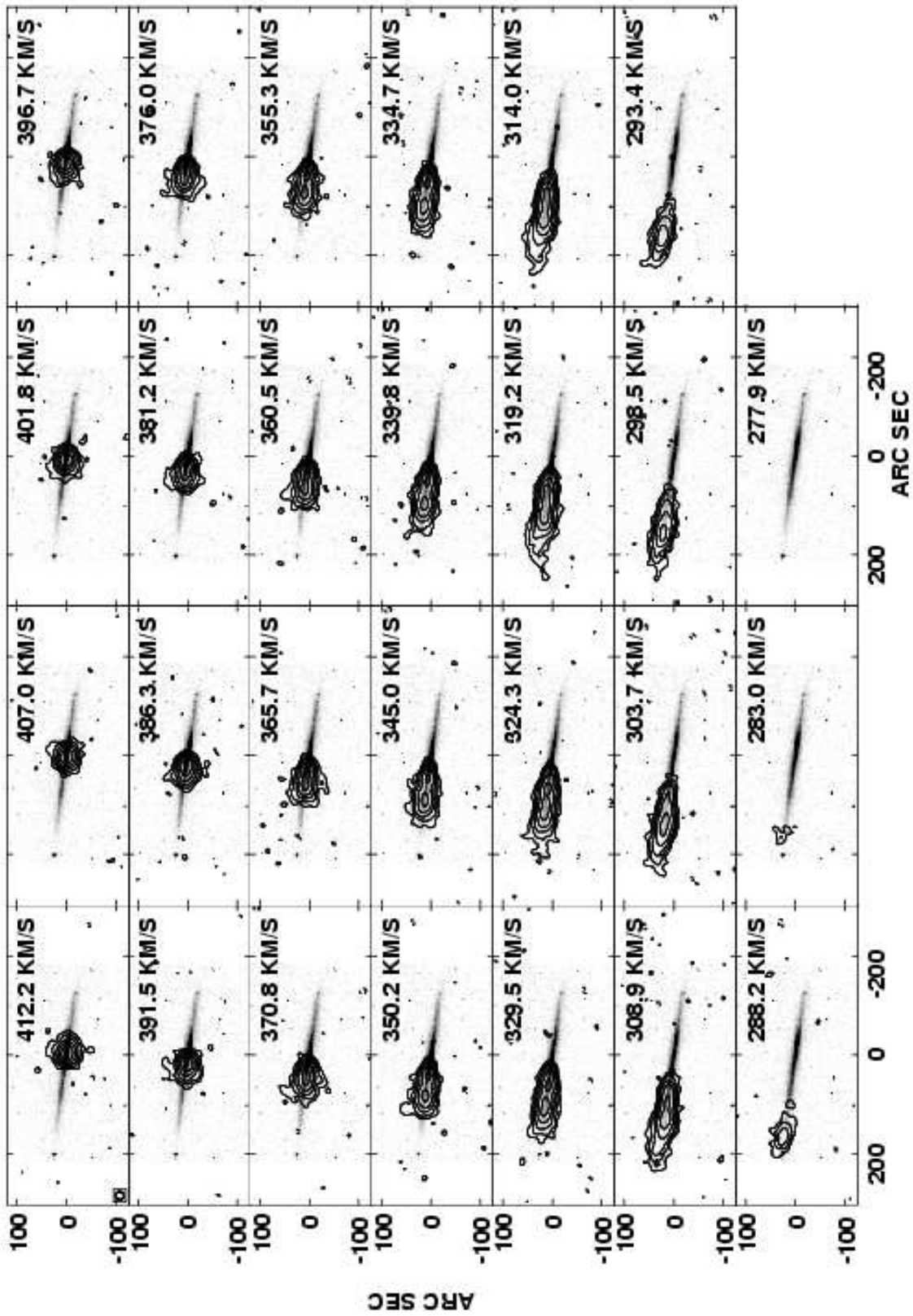


FIG. 5.— (continued)

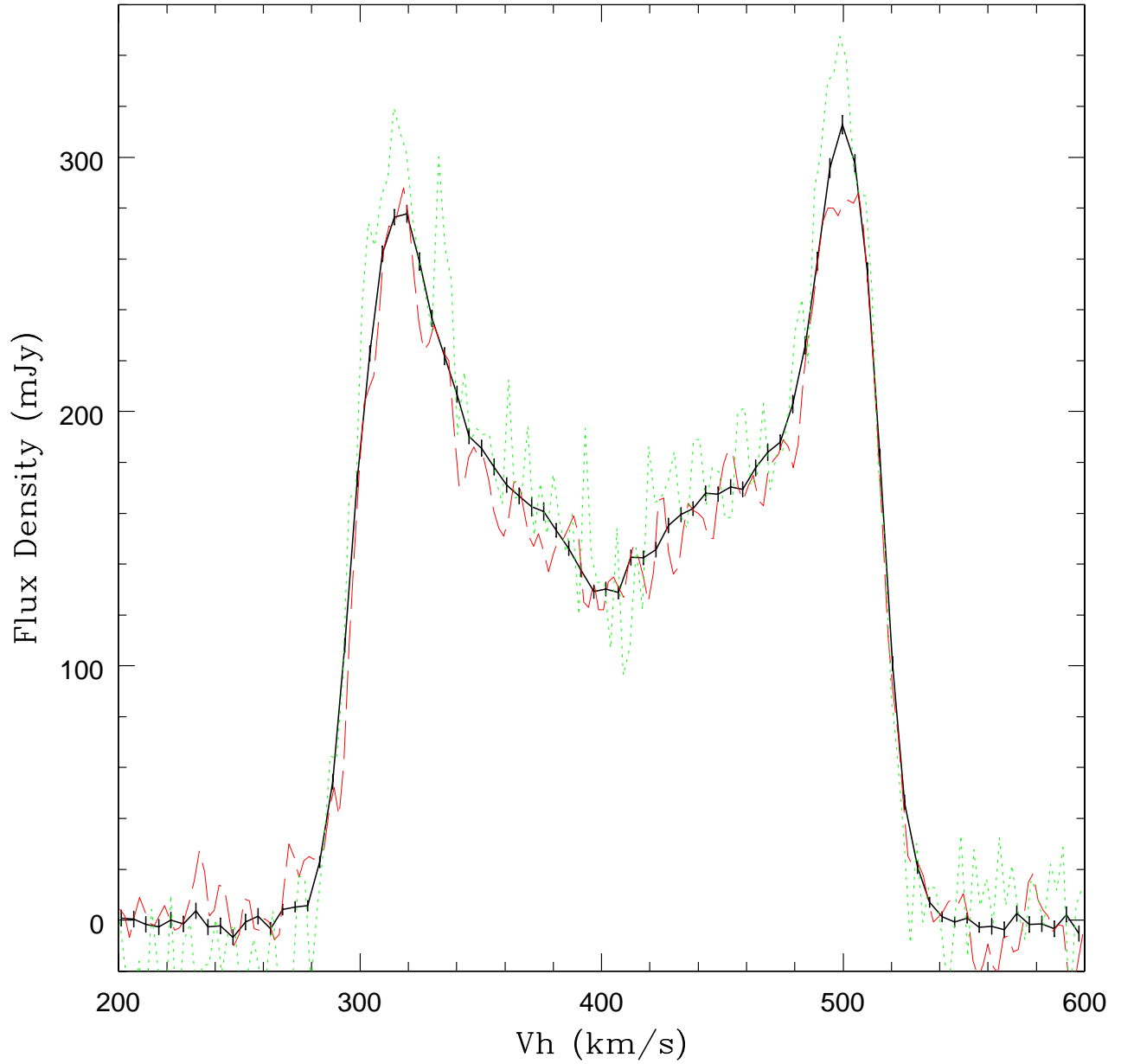


FIG. 6.— Global HI profile of UGC 7321 derived from our VLA data (solid line). The ( $1\sigma$ ) error bars are derived from the statistics of the images and do not include calibration and baseline uncertainties. Also shown are the global HI profiles measured with the NRAO 43 m. telescope (dashes; Haynes et al. 1998) and the Nançay telescope (dots; Matthews et al. 1999).

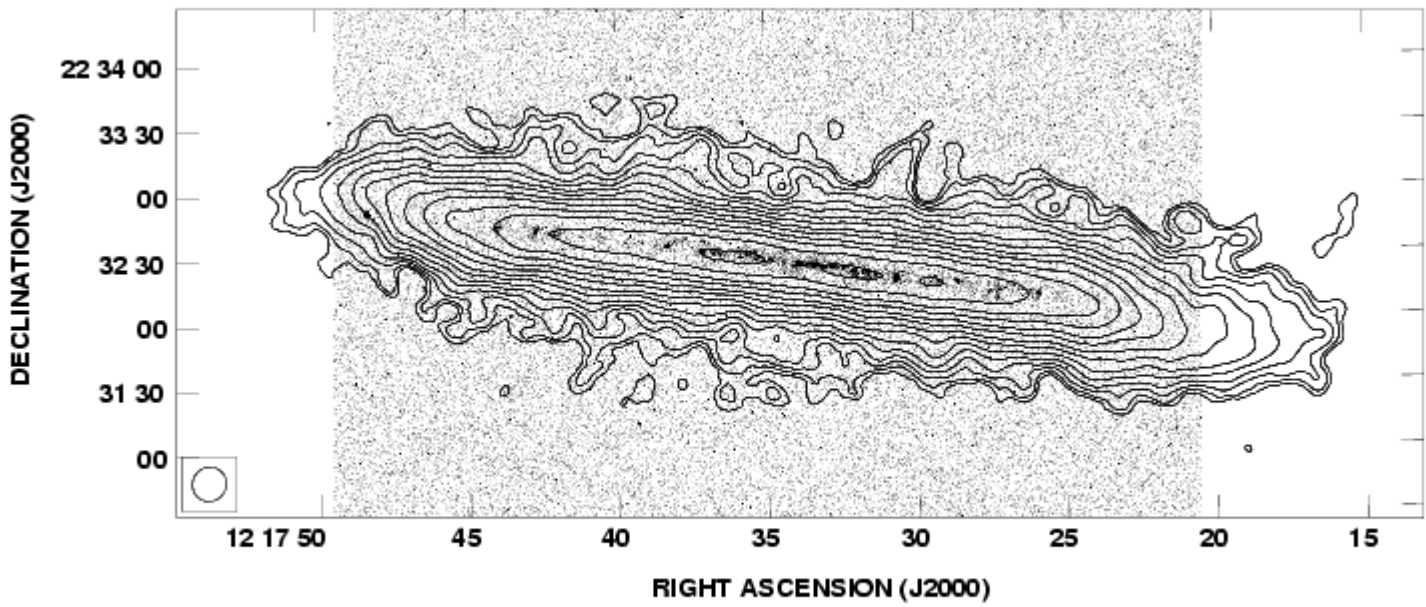


FIG. 7.— H I total intensity contours for UGC 7321, overplotted on an  $H\alpha + [N II]$  image of the galaxy from Matthews et al. 1999. The synthesized-beam is nearly circular with a FWHM  $\sim 16''$ . The contour levels are (-1 [absent], 1, 1.4, 2, 2.8, 4, 5.6, 8, 11, 16, 22, 32, 44, 64, 88)  $\times 18 \text{ Jy beam}^{-1} \text{ m s}^{-1}$ . The H I peaks at  $1661 \text{ Jy beam}^{-1} \text{ m s}^{-1}$ . Note the slight depression visible near the center of the disk as well as the “integral sign” shape seen in the outer H I contours, commencing near the edge of the stellar disk.

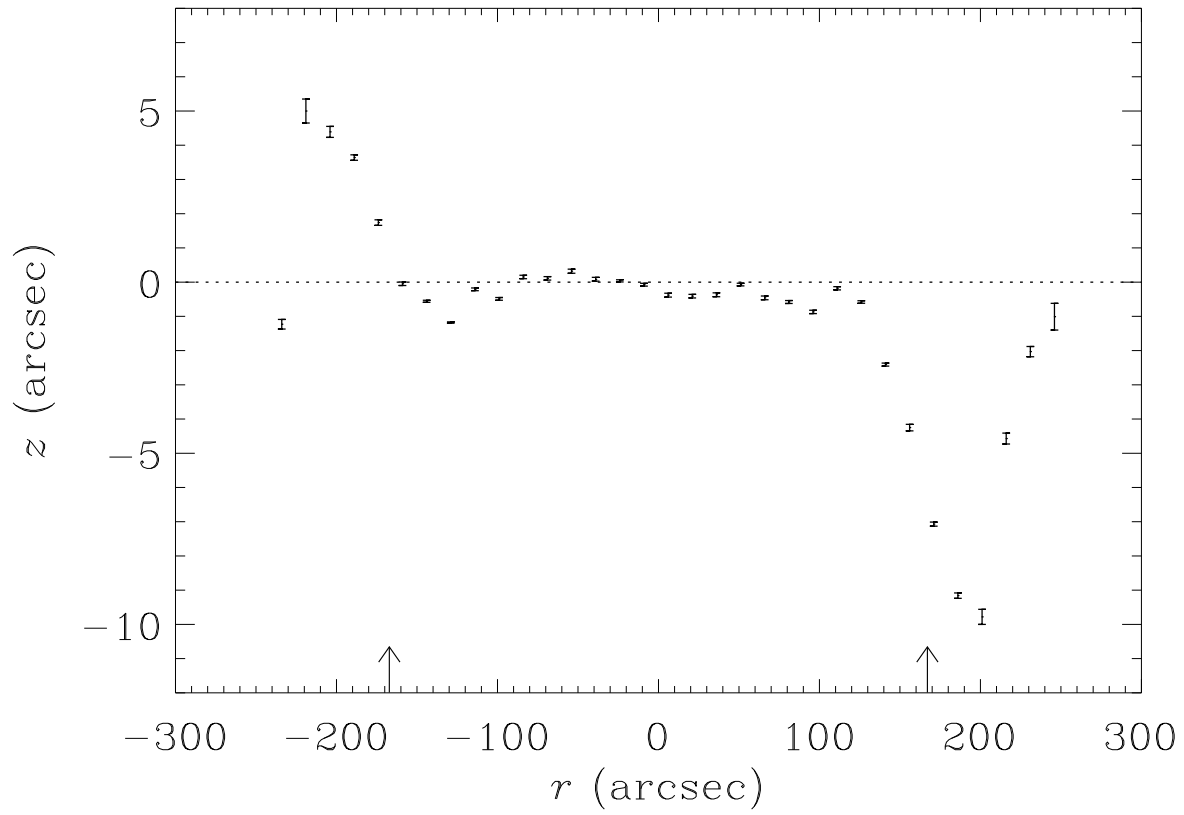


FIG. 8.— H I warp curve derived from UGC 7321 by fitting Gaussians to H I intensity profiles perpendicular to the major axis at various locations along the disk. The centroid of each fitted Gaussian is plotted at each fit location along with the  $1\sigma$  error bars derived from the formal uncertainty in the fit. Note that the warped material appears to curve back toward the equatorial plane in the outermost regions of the disk. The warp also shows a slightly different amplitude on the two sides of the disk. The arrows show the location of the observed edges of the stellar disk.



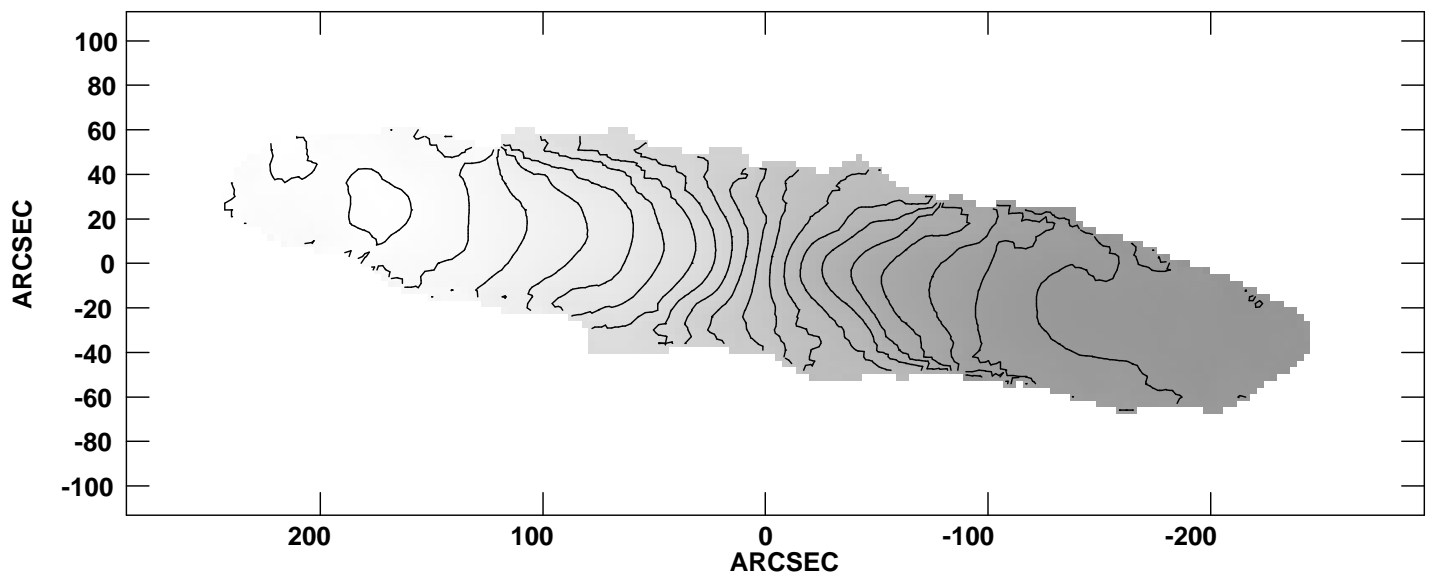


FIG. 9.— H I velocity field for UGC 7321. IsovLOCITY contours in the range  $(303.7\text{--}520.7) \text{ km s}^{-1}$  are shown (every second channel, see Figure 5), overplotted on a greyscale representation of the same map. The grey-scale is linear from  $303.7 \text{ km s}^{-1}$  (lightest) to  $520.7 \text{ km s}^{-1}$  (darkest).

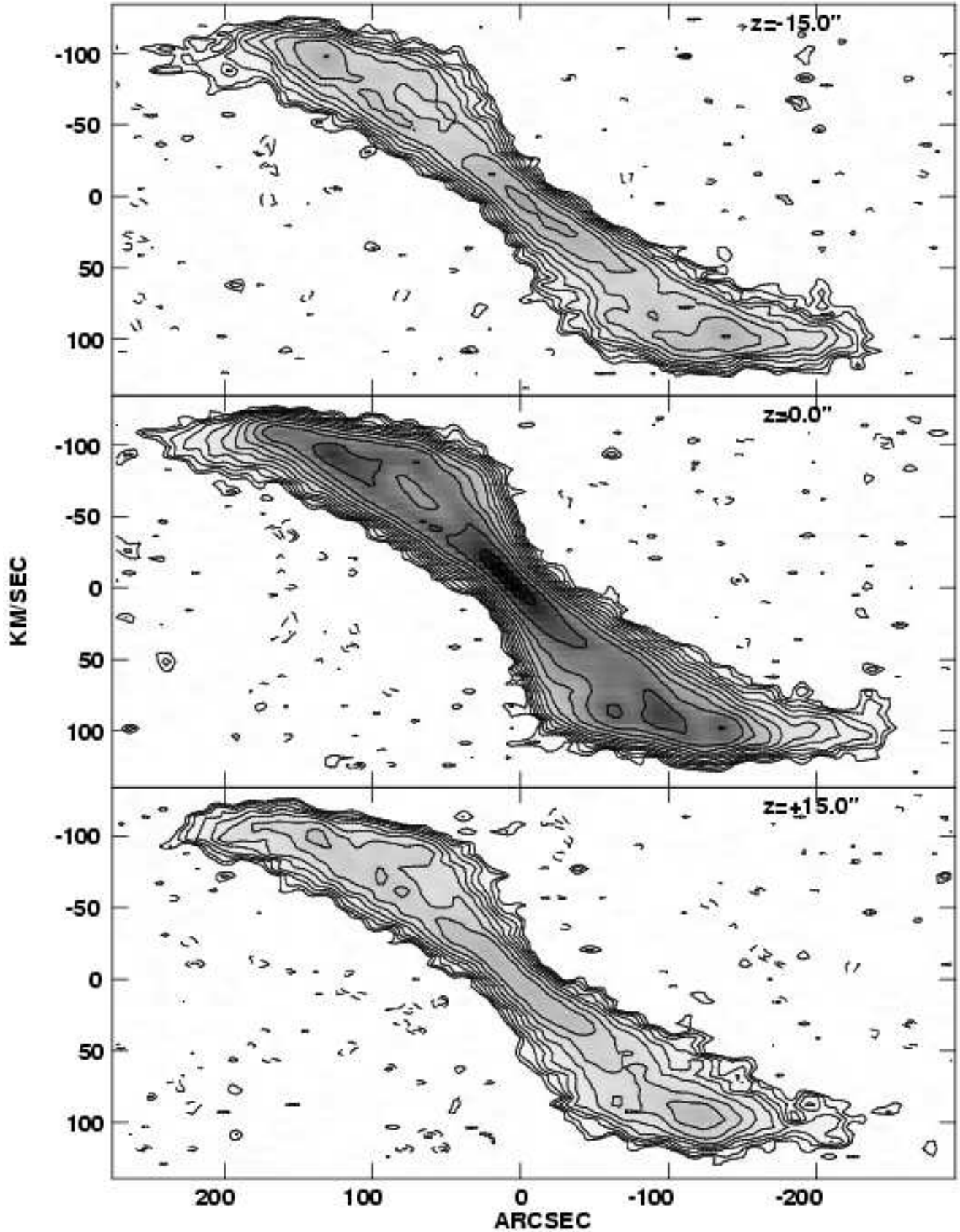


FIG. 10.— HI position-velocity (P-V) cuts parallel to the major axis of UGC 7321. These figures were derived from images with a spatial resolution of  $\sim 16''$  and a velocity resolution of  $\sim 5.2 \text{ km s}^{-1}$ . The cuts were extracted along the major axis and at  $z = \pm 15''$ . No averaging was applied along the  $z$  direction. The horizontal axis measures distance to the minor axis of the galaxy. The intensity shown is linear in the range (0–41) mJy/beam. The contour levels are: (-1.4 [absent], -1, 1, 1.4, 2, 2.8, 4, 5.6, 8, 11, 16, 22, 32, 44)  $\times 0.8$  mJy/beam.

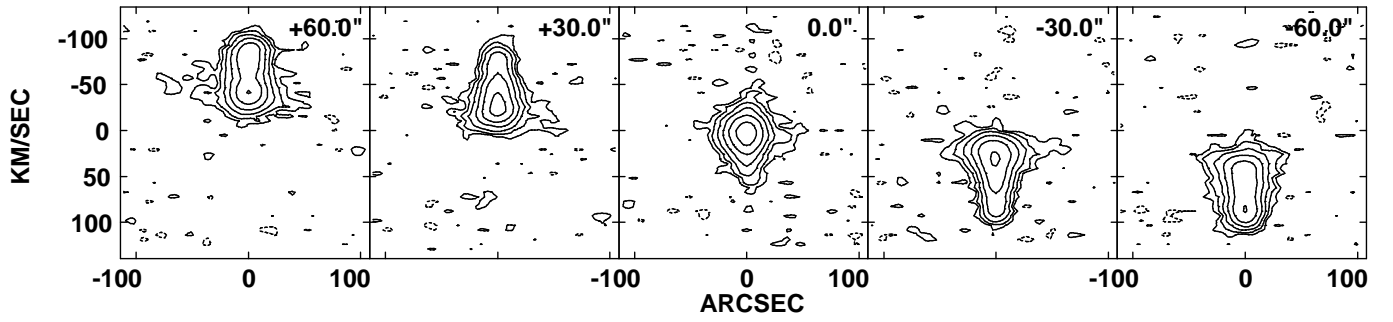


FIG. 11.— Position-velocity (P-V) plots at 5 locations parallel to the minor axis of UGC 7321. These figures were derived from images with a spatial resolution of  $\sim 16''$  and a velocity resolution of  $\sim 5.2 \text{ km s}^{-1}$ . The center panel shows the P-V cut along the minor axis; the other panels show cuts at positions  $r = \pm 30''$  and  $r = \pm 60''$ . No averaging was applied along the  $r$  direction. The horizontal axis measures the height above and below the midplane. The contour levels are:  $(-2 \text{ [absent]}, -1, 1, 2, 4, 8, 16, 32, 64) \times 0.8 \text{ mJy/beam}$ .

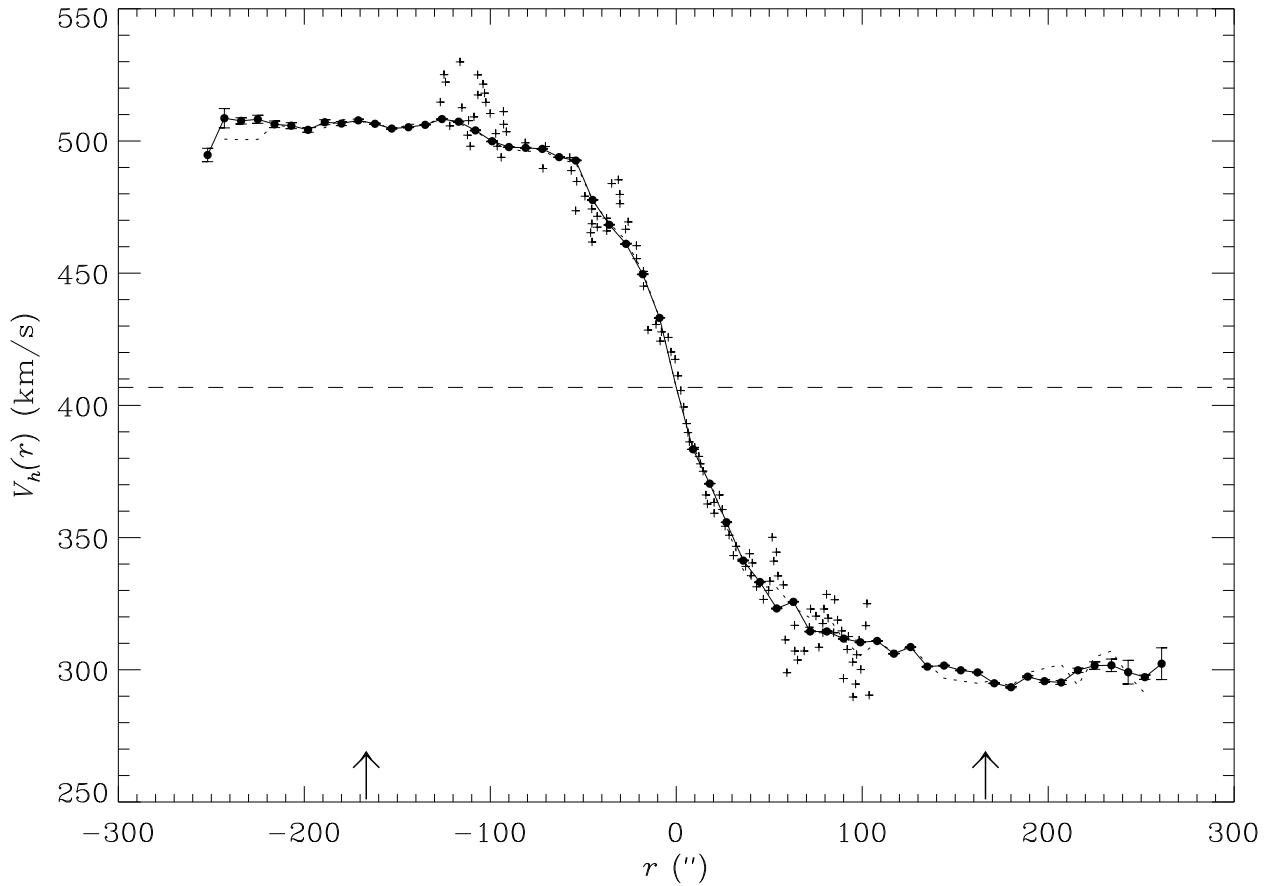


FIG. 12.— HI rotation curve for UGC 7321 derived from data with resolution  $16''$  (solid line and dots) and  $12''$  resolution (dotted line). The crosses were derived by Goad & Roberts (1981) using  $H\alpha$  emission-line spectroscopy. The axes are the distance from the center of the disk and the heliocentric rotational velocity. The horizontal dashed line indicates the systemic velocity inferred from the global HI profile (Section 5.3.1). The location of the observed edges of the stellar disk are indicated with arrows.

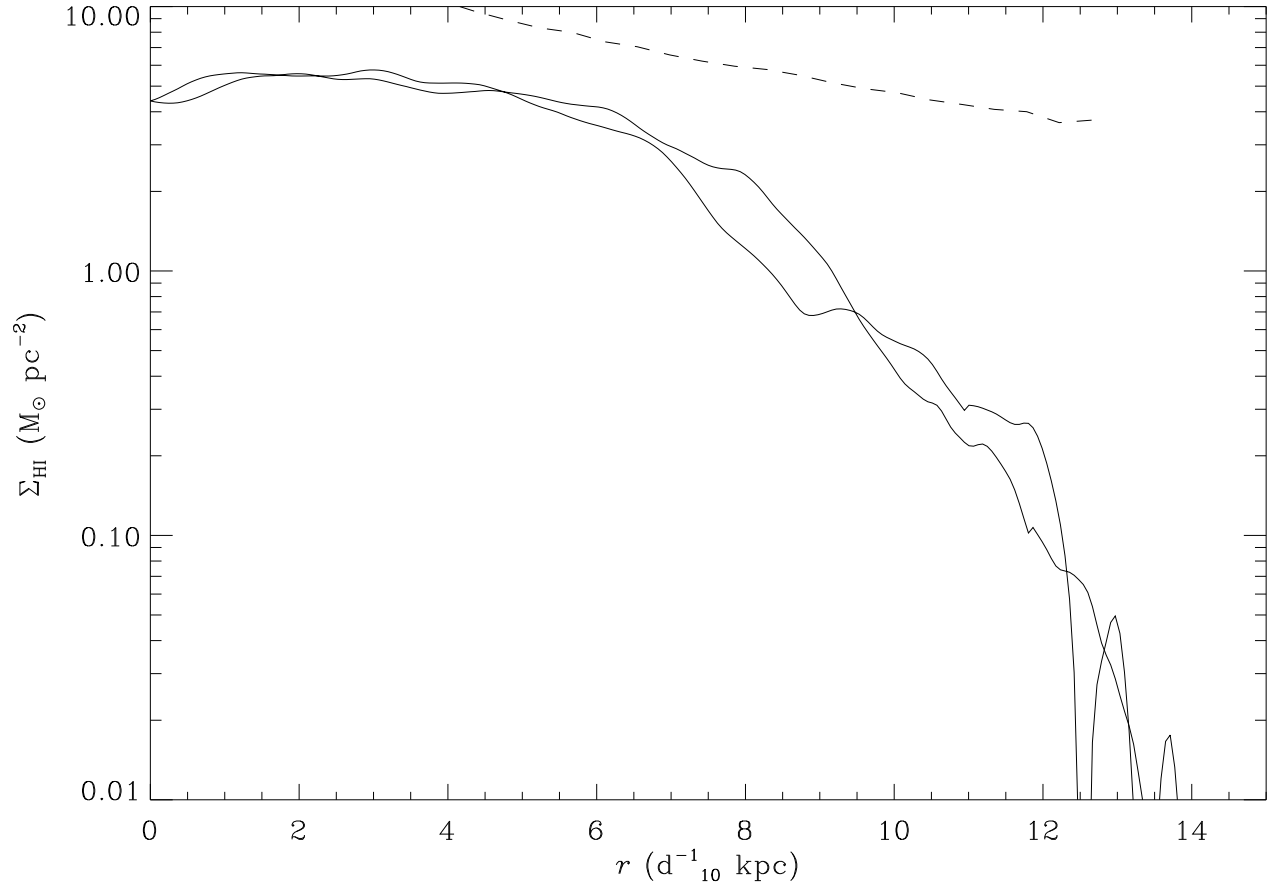


FIG. 13.— Deprojected radial HI profile along the major axis of UGC 7321, folded about  $r = 0$  (solid lines). The units are galactocentric radius (in  $d_{10}^{-1}$  kpc) and HI surface density (in  $M_{\odot} \text{pc}^{-2}$ , logarithmic scale). Overplotted as a dashed line is the critical HI surface density for star formation according to the dynamical criterion of Kennicutt 1989 (see text).